Roland Schmied, BSc

Fundamental proximity effects for electron beam induced deposition processes

MASTER THESIS

For obtaining the academic degree
Diplom-Ingenieur

Master Programme of
Technical Physics

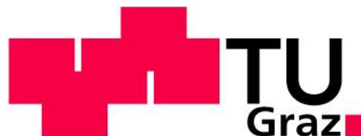

Graz University of Technology

Supervisor:

Ao.Univ.-Prof. Dipl.-Ing. Dr.techn. Ferdinand Hofer
Institute for Electron Microscopy

Graz, June 2011

Abstract

Electron beam induced deposition (EBID) is a powerful direct write method for 3-dimensional fabrication of functional nanostructures even on non-flat surfaces which has already found its way to commercial applications. EBID processing works with gaseous precursors which are locally decomposed on the surface by the focused electron beam into volatile (pumped out) and non-volatile fragments (functional deposit). The main problems of EBID, however, are low efficiencies, which result in time intensive processes, chemical impurities, which influence the intended functionalities, and unwanted proximity deposition due to electron trajectories in solids. However, the ongoing demand for even smaller structures requires a closer look to the intrinsic limitations of the EBID to exploit the full potential of this rapid prototyping technique.

In this master thesis, proximity deposition is characterized in detail which allows for a comprehensive insight to their formation processes. The study enables the separation of design and process related influences from fundamental limitations. Furthermore, since the functionality is of particular importance for electrically conductive deposits, the proximity deposition is characterized with respect to their chemical and physical properties. By combining the gathered results, it is possible to derive design rules for electron beam induced Pt deposits for a sub-100 nm height regime in order to minimize unwanted proximity deposition. Moreover, the study is of general interest for electron beam induced processes due to the fundamental approach for explaining the formation processes.

Kurzfassung

Elektroneninduzierte Abscheidung (EBID) ist eine leistungsfähige direkte Schreibmethode um funktionelle, 3-dimensionale Nanostrukturen selbst auf nicht ebenen Oberflächen herzustellen. Diese Methode wird bereits für kommerzielle Anwendungen genutzt. Beim elektroneninduzierten Abscheideprozess wird ein Precursormolekül aus der Gasphase durch einen fokussierten Elektronenstrahl lokal auf der Oberfläche in flüchtige (abgepumpt) und nicht flüchtige Fragmente (funktionelle Abscheidung) aufgespalten. Die größten Probleme dieser Methode sind vor allem die niedrige Effizienz, wodurch eine hohe Prozesszeit ensteht, chemische Unreinheit, welche der gewünschte Funktionalität entgegenwirken, und ungewünschte zusätzliche Abscheidungen, welche auf die Elektronentrajektorien im Festkörper zurückzuführen sind. Die Anforderungen nach immer kleineren Strukturen macht es nun notwendig die intrinsische Begrenzung dieser Methode näher zu betrachten um das ganze Potential dieser Technik nutzen zu können.

In dieser Master Arbeit werden die zusätzlichen kollateralen Abscheidungen charakterisiert, wodurch man einen Einlick in den Formierungsprozess dieser unerwünschten Effekte erhält. Die Studie ermöglicht es, die design- bzw. prozessbedingten Einflüssen von den fundamentalen Begrenzungen zu trennen. Aufgrund der immensen Bedeutung der Funktionalität von elektrisch leitfähigen Abscheidungen, werden die unerwünschten Nebeneffekte auf ihre chemischen und physikalischen Eigenschaften untersucht. Durch die Korrelation der unterschiedlichen Ergebnisse is es möglich, Designregeln für die elektroneninduzierte Pt Abscheidung, für Höhen bis zu 100 nm, aufzustellen um die unerwünschten Abscheidungen zu minimieren. Weiters ist die Arbeit von allgemeiner Bedeutung für elektroneninduzierte Abscheidungen, da für die Erklärung der Formierungsprozesse der unerwünschten Nebeneffekte elementare Aspekte diskutiert werden.

Acknowledgements

First of all, I'd like to thank Professor Ferdinand Hofer for providing the framework and the financial support for this thesis at this sophisticated institute.

I want to thank Harald gratefully for his inimitable way of introducing me into the field of scientific work and the successive, but effective and successful discussions, revealing the far-ranging wideness of science.

I also want to thank the whole FELMI and ZFE stuff, especially Ilse, Sanya, Christian and Herbert for their kind admitting, their helpful support and the friendly atmosphere.

Furthermore, I want to thank the Christian Doppler Research Association (CDG), Isovoltaic GmbH and the Federal Ministry of Economy, Family and Youth of Austria for financial support.

Most importantly, I want to thank my parents, for their love, and for giving me the chance of making these academic studies.

Table of Contents

Abstract ii

Kurzfassung iii

Acknowledgements iv

List of abbreviations ix

Motivation xi

Outline xiii

1 Fundamentals and Methodology 1
- 1.1 Electron beam induced deposition 1
  - 1.1.1 Components 2
  - 1.1.2 Fundamental principle 4
- 1.2 Atomic force microscopy 14
  - 1.2.1 Components 14
  - 1.2.2 Topographical imaging 18
  - 1.2.3 Kelvin Probe force microscopy 22
  - 1.2.4 Conductive AFM 25
- 1.3 Experimental details 26
  - 1.3.1 Electron beam induced deposition - details 26
  - 1.3.2 Atomic force microscopy - details 32
  - 1.3.3 Simulations 36

2 Results 38
- 2.1 Representative characterisation of halo effects 40
- 2.2 Electron energy and height variation 47
  - 2.2.1 Outer halo development 49
  - 2.2.2 Edge halo and inner halo development 51
  - 2.2.3 KPFM comparison 56
  - 2.2.4 Conductive AFM measurements 59

3 Discussion 62

4 Summary 69

List of Figures

1 Possible application for EBID . . . xi

1.1 Schematics of EBID . . . 1
1.2 Schematic SEM drawing . . . 2
1.3 Electron beam distribution . . . 3
1.4 Elements available for EBID . . . 5
1.5 Working principle of EBID . . . 5
1.6 Schematic drawing of BSE contributing to deposition . . . 6
1.7 Elastic and inelastic scattering . . . 7
1.8 Electron energy spectrum . . . 7
1.9 Electron cross section for CF_4 . . . 9
1.10 Deposition events by different electrons . . . 10
1.11 Gas distribution at surface . . . 11
1.12 Optimized GIS geometry . . . 11
1.13 Dwell time limitation . . . 12
1.14 Dwell time limitation . . . 12
1.15 Diffusion limited regime . . . 13
1.16 Gas flux limited regime . . . 13
1.17 Schematic design of a tube scanner . . . 15
1.18 Schematic working principle of PSD . . . 16
1.19 SEM picture of AFM tip . . . 17
1.20 Comparison of fine and dull tip . . . 17
1.21 Comparison of tetragonal and radial tip . . . 18
1.22 Lennard-Jones potential . . . 19
1.23 Schematic possible damage caused by tip . . . 20
1.24 Schematics of excitatoin of cantilever . . . 21
1.25 Approached AFM tip . . . 21
1.26 Energy levels at KPFM . . . 23
1.27 Contributions to KPFM measurement . . . 24
1.28 Used SEM/FIB Dual Beam Microscope . . . 26
1.29 Chemical formula of used precursor gas . . . 27
1.30 Used precursor with fragments . . . 27
1.31 Bright field TEM image of Pt-nanorod . . . 28
1.32 Scan array . . . 29
1.33 Stream file generated . . . 29
1.34 Structure alignment on substrates . . . 30

1.35 Structure arrays for different electron energies 31
1.36 Structure alignment on conductive path 32
1.37 Dimension 3100 AFM 33
1.38 Active sample holder 35
1.39 Signal access box 36

2.1 Height and KPFM image of the structure 38
2.2 Concept of deposition 39
2.3 Height vs. loop number at 20 keV 40
2.4 Height and KPFM plot 30 keV 41
2.5 Outer halo radius 30 keV 42
2.6 H_{edge} at 30 keV 43
2.7 H_i at 30 keV 43
2.8 Geometric tip limitation 44
2.9 KPFM image and line section 45
2.10 KPFM cross line section and closer look to the H_i 46
2.11 Height sections for all energies 48
2.12 Outer halo all energies 50
2.13 H_{edge} at all energies 51
2.14 H_i at all energies 52
2.15 Forward scattering contribution 53
2.16 CASINO simulation on 100 nm Ti 54
2.17 Contribution to FSE per loop 56
2.18 KPFM sections for all energies 58
2.19 3D image of C-AFM measurement 59
2.20 Topography and C-AFM image 60

3.1 Concept of deposition 62
3.2 Deposition events by different electrons 63
3.3 Results for all halo and all energies 64
3.4 Results for edge and inner halo 65
3.5 KPFM cross line section and closer look to the H_i 67

List of Tables

1.1 AFM tip properties 16
1.2 Interaction between tip and surface 18
1.3 Summary of conductive coatings 25
1.4 Properties of used precursor gas 27
1.5 Summary of used parameters 30
1.6 Summary of used tips 34

2.1 Summary of height vs. loop number functions, derived from AFM measurements. (h... height (nm), l...loop number) 47
2.2 Outer halo radius 49
2.3 Radius of electrons contributing to forward scattering 53
2.4 Radius of electrons contributing to forward scattering 55

List of abbreviations

$^\circ$	degree
μm	micrometer
μs	microseconds
AFM	atomic force microscopy
Au	gold
BSE	backscattered electrons
C	carbon
C-AFM	conductive atomic force microscopy
CF_4	tetrafluoromethane
CVC	current-voltage converter
D	diffusion coefficient
ΔV	potential difference
DA	diffusion assisted
e	elementary charge
E_0	primary electron beam energy
EBID	electron beam induced deposition
eV	electron volts
F_{es}	electrostatic force
FEG	field emission gun
FIB	focussed ion beam
FWHM	full width at half maximum
GL	gas flux limited
H_{edge}	edge halo
H_i	inner halo
H_o	outer halo
I_p	beam current
J	gas flux
keV	kilo electron volts
kHz	kilohertz
KPFM	kelvin probe force microscopy

MTL	mass transport limited
n(r)	number of adsorbed molecules per surface unit
n/n_0	coverage
nm	nanometer
pA	picoampere
PE	primary electrons
ϕ_{tip}	working function of the tip
ϕ_{sample}	working function of the sample
PSD	position sensitive detector
Pt	platinum
PtIr	platinum iridium
Q	quality factor
r_{BSE}	surface radius of BSE
RMS	
RRL	reaction rate limited
s	sticking probability
SAB	signal access box
SE	secondary electrons
SEM	scanning electron microscopy
Si	silicon
$\sigma(E)$	electron impact dissociation cross section
SiO_2	silicon oxide
τ	residual time
Ti	titanium
TiN	titanium nitride
UHV	ultra high vacuum
V	volume
V_{AC}	alternating currend voltage
V_{CPD}	contact potential difference
V_{DC}	direct-current voltage
V_{LJ}	Lennard-Jones potential
V_{rep}	repulsive Pauli interaction
V_{vdW}	van der Waals potential
W_2C	tungsten carbid

Motivation

Over the last decades various structuring techniques have been developed for nanoscale fabrication, e.g. UV-, X-ray of electron beam lithography. By reaching their limits, novel approaches have been developed.

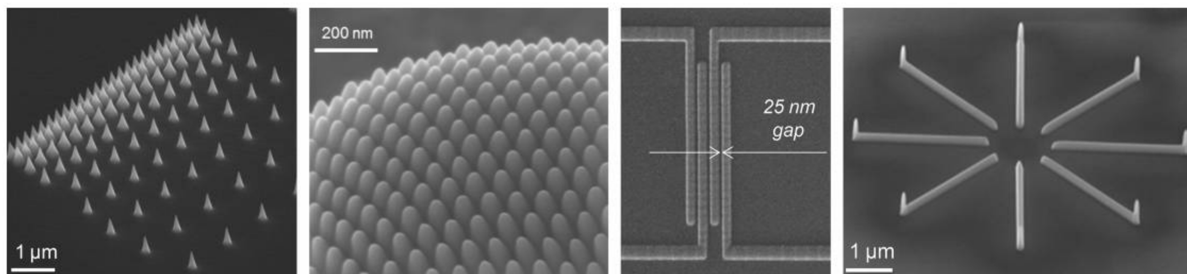

Figure 1: Different applications of EBID. On the left side one can see a multiple tip surface with varied distances. On the second image one can see a structure deposited on a non-flat surface. The third image shows a nanoscale 4 point structure and on the last image one can see a MEMS structure.

During the last years focused electron beam induced deposition (**EBID**) from the gas phase has attracted more and more attention since it represents a very powerful direct write method for the 3-dimensional fabrication of functional nanostructures (conductive, insulating, magnetic,) even on non-flat surfaces, possible applications are shown in figure 1. In contrast to focused ion beam (**FIB**) assisted deposition, which is an often used technique, EBID is free of sputtering effects, unwanted ion implantation, and the partly high thermal stress which can alter or harm the substrate. By the variation of the used precursor gas, the functionality of the deposit can be manipulated, ranging from insulating over magnetic towards conducting such as W, Au or Pt. Due to these advantages, EBID is highly suited for rapid prototyping with particular emphasis to sensitive samples such as soft matter (polymers, biological samples,), nanoelectronic applications or proof of concept studies.

Hence, EBID suffers from three main problems: 1) low efficiencies which make EBID

time intensive; 2) chemical impurities, mostly carbon, which influences the intended functionality; and 3) proximity deposition due to the electron trajectories in solids.

However, the ongoing demand for even smaller structures requires a closer look to the constraints of EBID in terms of spatial resolution and their conductivity. To do so, a separation of design and process related influences from fundamental limitations is needed, which is subject of this thesis, and design rules are deduced for minimizing these influences.

The studies have been performed with a widely used Pt precursor gas and subsequently investigations via atomic force microscopy, Kelvin probe force microscopy, conductive atomic force microscopy and scanning electron microscopy to provide a comprehensive insight. Although carried out with one specific precursor material, the study is of general interest for all EBID related processes due to the fundamental aspect of electron propagation in solids.

Outline

- In chapter 1 the basics of the electron beam induced deposition process (section 1.1) is described with the components needed and the fundamental principle of this process.
- In the next section a description of the method of atomic force microscopy (section 1.2) is given. Beside the fundamental topographical imaging, Kelvin probe force microscopy and conductive AFM is described.
- In section 1.3 the used microscopes and methods of deposition and investigation with FIB and AFM are described.
- In the next part, chapter 2, the different halos are classified followed by a detailed presentation of the gathered results.
- In the last chapter 3, the results are discussed, from which the design rules are derived.

1 Fundamentals and Methodology

1.1 Electron beam induced deposition

As the request for ever finer dimension patterning has been arisen, e.g. the micro- and nanofabrication in the integrated circuit industry, nonplanar techniques of fabrication have been developed firstly for research application, but also for potentially novel manufacturing processes [1]. One of these techniques is electron beam induced deposition (**EBID**), where a focussed electron beam impinges the substrate surface, at which the deposition gas is floated.

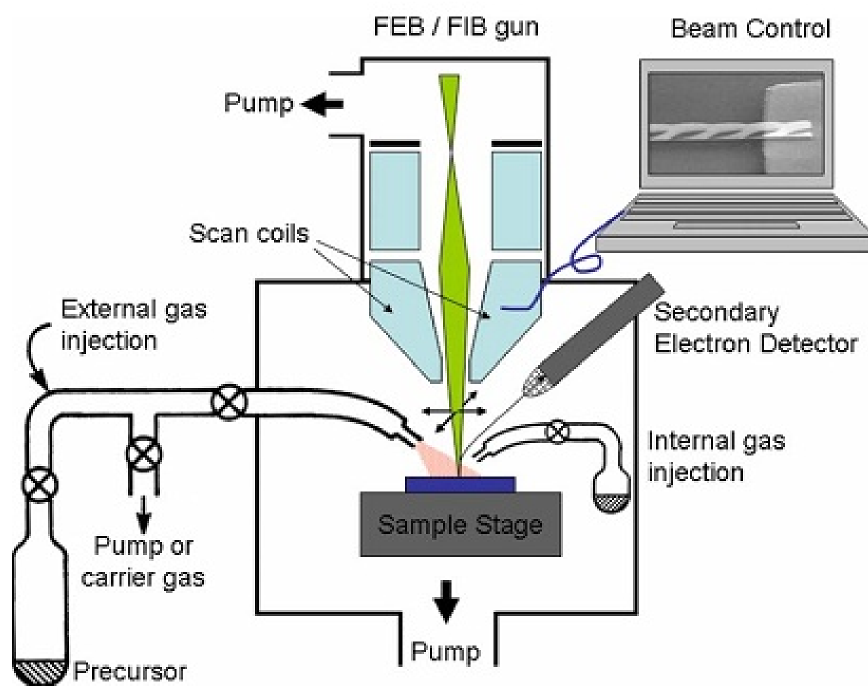

Figure 1.1: Schematic Design of an electron beam induced deposition. [1]

As one can see in figure 1.1 there are two essential parts: 1) the electron beam; 2) the precursor gas itself with the gas injection system. These components are discussed in

the following section in detail.

1.1.1 Components

Electron beam

The first essential part for electron beam induced deposition is the electron beam itself. The electron column ispractically identical to a classical scanning electron microscope (**SEM**) [2] and consists of an electron point source, followed by some electron lenses with apertures, which are responsible for demagnifying the point source onto the sample surface, and finally the scan coils, which move the electron beam systematically over the surface (see figure 1.2)[2].

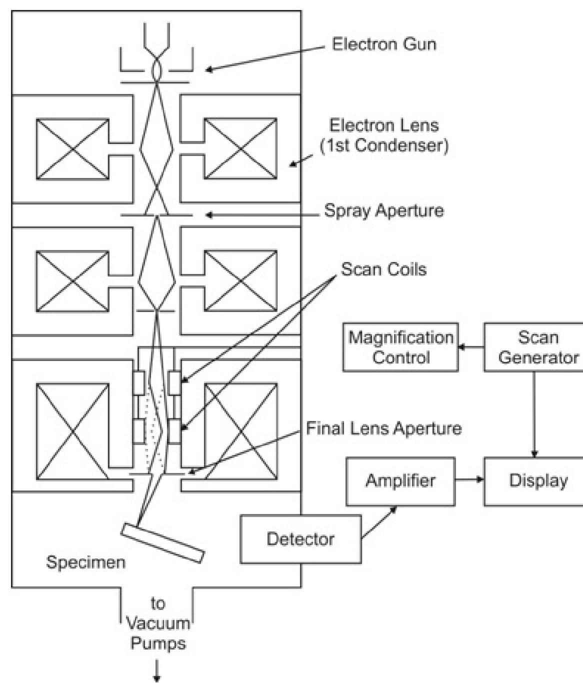

Figure 1.2: Schematic SEM drawing. [3]

The main parameters for the electron beam are the acceleration voltage (electron energy), the beam current and the beam diameter impinging on the sample. The acceleration voltage can typically be variied between 0.5 and 30 keV.

The electron columns used for EBID allow beam diameters down to about 1 nm [4]. The higher the acceleration voltage, the smaller the beam diameter can be, which depends also on the working distance. Usually, at smallest working distances it gets

otpimized, but the working distance can't be minimized, because there has to be space for the gas injection system [1].

Neglecting astigmatism and abberation [2], the electron beam cross section can be well described by a Gaussian distribution ($f(r)$ is in electrons per unit area and time, a is the standard deviation, I_p is the beam current, and e is the elementary charge):

$$f(r) = \frac{I_p/e}{2\pi a^2} \exp(-\frac{r^2}{2a^2}) \tag{1.1}$$

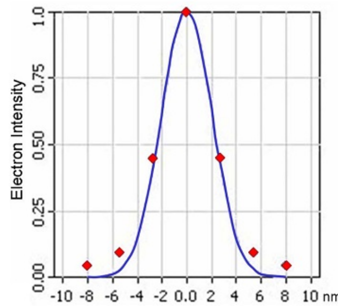

Figure 1.3: Measured electron beam distribution (20 keV) and Gaussian for FWHM = 4.4 nm. [5]

With this Gaussian distribution the beam size definition isn't uniform. It can be defined at $1/e$, $1/e^2$, the full width at half maximum (**FWHM**) or full widths comprising 50% or 90% of all electrons.

Another important parameter is the beam current. With this parameter the average time between two incident particles is preassigned. This average time is important for EBID, because of the gas diffusion related replenishment to the actual area of deposition [1], [6], [7], [8]. So the beam current affects the effective deposition rate, due to current dependent local depletion [9], [10], [1], [8].

Precursor gas

The used precursor gas depends on the material intended to be deposited on the surface [11]. On the one hand this gas should stick to the surface and remain there to be dissociated for deposition, but on the other hand the dissociated, unwanted fragments should be highly volatile [1], [11].

To bring the precursor gas to the surface a special gas injection system is used [1].

Such systems contain the precursor material in a reservoir, where it can be heated above their respective melting points, to provide the material in a stable gas phase. A long, thin needle with a inner diameter of approximately 500 nm is then placed closely, approximately 200 μm, above the surface to supply the surface with a locally high gas flux [12].

For a sophisticated deposition process the quality of vacuum is essential. Since water is known to chemisorb on most surfaces, water and hydrocarbons will influence the results of deposition as a result of an unwanted background pressure. Hence the purity of obtained deposition is dependent on the vacuum quality [13].

Another important parameter of the precursor gas is the vapour pressure, which accounts for the amount of molecules evapourated from the reservoir and further transported to the substrate surface [12].

Since EBID covers a wide range of applications, the used precursor gases are quite numerous, but they all are generally composed of a central atom/ion and ligands. The whole complex has to be uncharged, because otherwise the volatile character will be lost [1]. Furthermore, it should not have a strong dipole moment or be polarized easily to be volatile. However, for sticking onto the surface, these properties would be useful. Some commonly used precursor gases are organic compounds for C deposition, hydrides, halides, carbonyls, organometallics or oxide deposistion precursors. A list of material available for deposition is shown in figure 1.4 including the so far highest material content (at. %) within the solid whereby most benchmark needed special post-procedures to achieve such results [11].

1.1.2 Fundamental principle

As briefly described above, EBID uses a focussed electron beam for dissociation onto the substrate surface. For a successfull material deposition, the precursor gas has to be adsorbed and must be dissociated by the impinging electrons or by subsequent processes. A scheme of the working principle is shown in figure 1.5.

The dissociation rate will be dependent on the surface density of electrons and precursor molecules as well. The vertical deposition rate can be described for a rotational symmetry in dependency of the distance r from the center of the primary electron beam [15]:

													C 100%				
												Al ★	Si 100%				
			Ti 35%		Cr ★	Mn ⊗	Fe 100%	Co 97%	Ni 36%	Cu 60%		Ga 50%	Ge 100%				
					Mo 10%		Ru ⊗	Rh 66%	Pd >50%				Sn 58%				
					W 66%		Os ⊗	Ir 33%	Pt 83%	Au 100%			Pb ⊗				

Figure 1.4: Elements available for EBID, including the best purities obtained in at.%. For ⊗ - marked elements there is no quantitative information on the composition available. Materials marked with a ⋆ are deposited pure. [11]

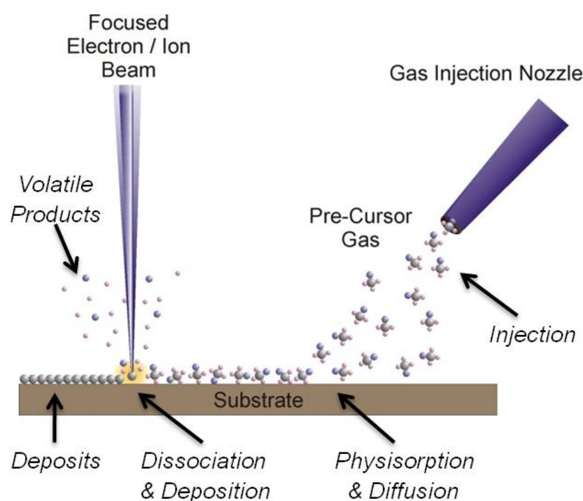

Figure 1.5: Schematics of the working principle of EBID. [14]

$$R(r) = Vn(r) \int_0^{E_0} \sigma(E) f(r, E) dE, \tag{1.2}$$

with V the volume of the decomposed molecule, $n(r)$ the number of adsorbed molecules per surface unit, $\sigma(E)$ is the electron impact dissociation cross section and E_0 is the energy of the primary electron beam.

The adsorption of precursor molecules can be described by four processes. First of all there is the adsorption from the gas phase influenced by the gas flux J, the sticking

probability s, and the coverage n/n_0. The second process is the diffusion on the surface to electron beam impinged areas from untasted ones, dependent on diffusion coefficient D and the concentration gradient. The third process is the spontaneous thermal desorption after residual time τ. The last and most important process is the molecule dissociation of the electron beam itself. These processes can mathematically be described by the molecule adsorption rate $\partial n/\partial t$:

$$\frac{\partial n}{\partial t} = \underbrace{sJ(1-\frac{n}{n_0})}_{adsorption} + \underbrace{D(\frac{\partial^2 n}{\partial r^2} + \frac{1}{r}\frac{\partial n}{\partial r})}_{diffusion} - \underbrace{\frac{n}{\tau}}_{desorption} - \underbrace{\sigma f n}_{decomposition} \tag{1.3}$$

By solving the equations 1.2 and 1.3 one can calculate the spatial distribution of deposition rate [1].

Electron - surface interaction

A lack of the concept of equation 1.2 is, that no bulk processes, such as penetrating electrons, are considered. Besides direct interaction between the primary electron beam and the adsorbed precursor molecules, electrons reemitted from the surface can participate to deposition processes.

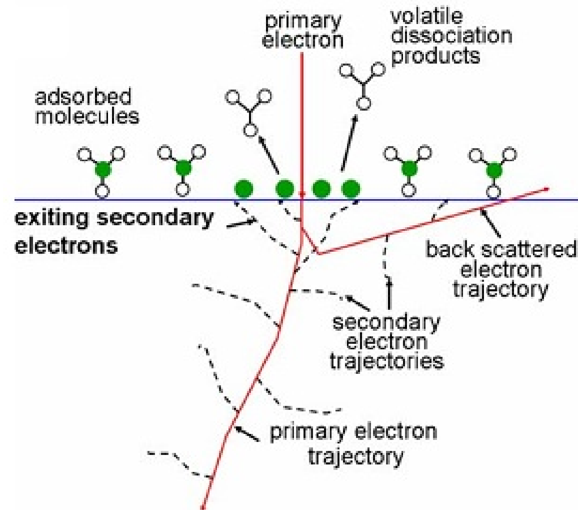

Figure 1.6: Scheme of electrons being reemitted from substrate and contributing to deposition. [1], modified

The primary electron beam penetrates into the substrate, depending on the sub-

strate material and electron energy ranging from micrometers down to a few nanometers. Within the substrate the electron path changes due to elastic and inelastic scattering [2].

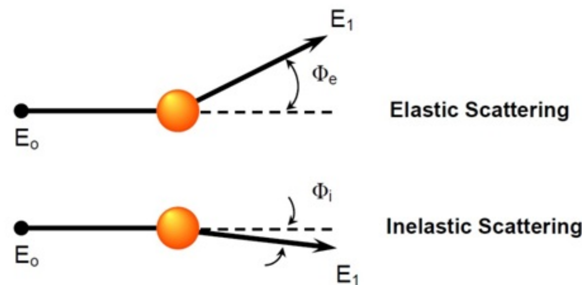

Figure 1.7: Schematic elastic and inelastic scattering. [3]

As shown in figure 1.7, the high angle scattering by the substrate atoms, where the energy is conserved, is called elastic scattering, whereas at an inelastic scattering event the incoming primary electron collides with an another electron and gets scattered by a low angle. It is called inelastic because energy can be transfered [2].

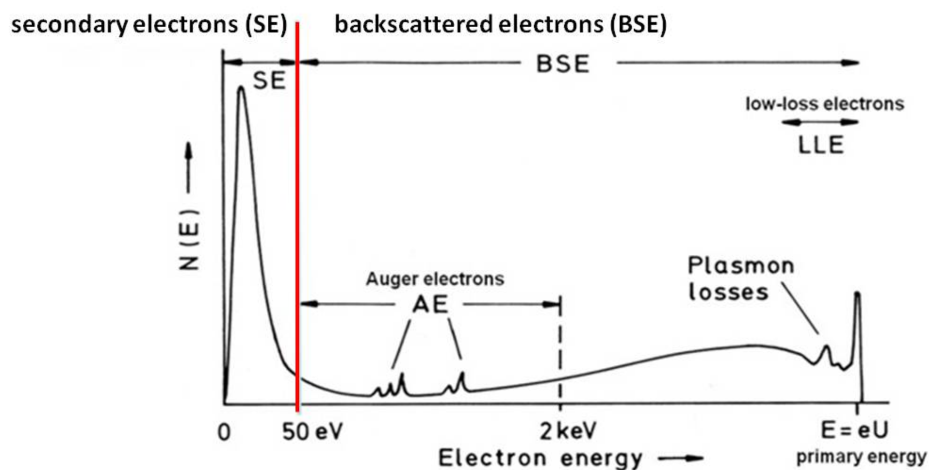

Figure 1.8: Energy spectrum of electrons from the primary electron beam. [3]

For primary electrons (**PE**) it is also possible to escape the substrate again. Electrons, which escapes the substrate/deposit due to elastic collisions in an angle of 0° to 90° from the electron beam are called backscattered electrons (**BSE**). If they escape the deposit in an angle ≥ 90°, they are called forward scattered electrons (**FSE**) . On the other hand there are the secondary electrons ($\mathbf{SE}_I$), which are generated by inelastic scattering events. At such a scattering event the primary electron looses a portion of his energy

and weakly bound outer shell electrons or conduction band electrons get this small amount of energy to escape from their initial point. On his way through the substrate a primary electron can produce many secondary electrons. So we get an energy spectrum ranging from the primary electron energy to almost 0 eV like qualitatively shown in figure 1.8 [16].

Secondary electrons are definded to have low energies below 50 eV, whereas the backscattered electrons can have energies up to the primary electron beam energy. Due to this energy difference the penetration depth is quite different. SE can only penetrate a few nanometers, typically $\leq$ 25 nm, whereas BSE can build an interaction volume up to a few micrometers. But SE are also found far away from the primary beam, because of the high energy of some BSE, they can also generate secondary electrons, which are then called SE_{II}. The FSE can also generate these type of electrons, which then are called SE_{III}. Besides PE, these three types (BSE, SE_{II} and SE_{III}) are also responsible for deposition.

Electron - molecule interaction

The electron - molecule interaction can be understood by numerous different mechanisms, such as dissociation, stimulated desporption, polymerisation or sputtering [1]. For each mechanism a cross section $\sigma(E)$ can be found, which is energy dependent. To simplify this problem one can use one cross section for all mechanisms. There also are differences between gas phase and adsorbed molecules [1].

One can find three dissociation mechanisms for gas phase molecules, as experiments on CF_4 show [17]. The first mechanism is dissociation through electron attachement. This process occurs at energies close to secondary electron energies, as one can see in figure 1.9 by the red graph. This peak has exactly the energy of the lowest unoccupied molecular orbital.
The second mechanism is the direct dissociation into ions. This cross section has an energy threshold, due to the ionization energy, as can be seen by the blue graph in figure 1.9. Its peak value is about 70-100 eV.
The third mechanism is direct dissociation into neutral atoms, for which the cross section looks quite similar to the ionization mechanism, with its threshold energy at the dissociation energy (molecule bond enthalpy), as shown in figure 1.9 by the purple graph.

For more complex precursor gases the fragments of dissociation due to ionization can

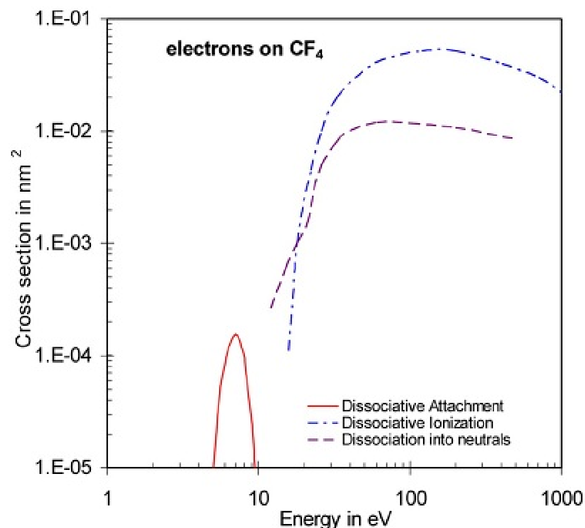

Figure 1.9: Electron impact total cross section for gas phase CF_4 [18].

end up in a variety of different molecules, for which it gets even more difficult to find a cross section for the deposition process.

The main differences between gas phase molecule - electron interaction and the interaction of electrons with adsorbed molecules is firstly that electrons will scatter in multiple events, penetrating through the substrate and being trapped or getting reflected back into vacuum. Due to this an cross section for a single scattering event is very complicated to find. The second major difference concerns the electronic relaxation, where some additional channels are provided in the adsorbed phase compared to the gas phase. A third difference is that dissociated molecules may react with neighbouring molecules in condensed films, which produced even more relaxation channels.

So at the substrate many different events contribute to dissociation. First of all the primary electrons (PE), but also back scattered and secondary electrons from the deposit (BSE_I, SE_I) are able to dissociated precursor gas molecules. Other electrons contributing are: forward scattered electrons (FSE), secondary electrons from the substrate surface, which can be sub-divided into two groups. The first one (SE_I) gets directly produced by forward scattered electrons and the second one (SE_{II}) gets produced by back scattered electrons (BSE_I) from the substrate, which also contribute to the deposition of precursor molecules.

As one can see, there are many different electron species, which can contribute to the deposition. These leads to proximity effects in the surrounding area of the primary

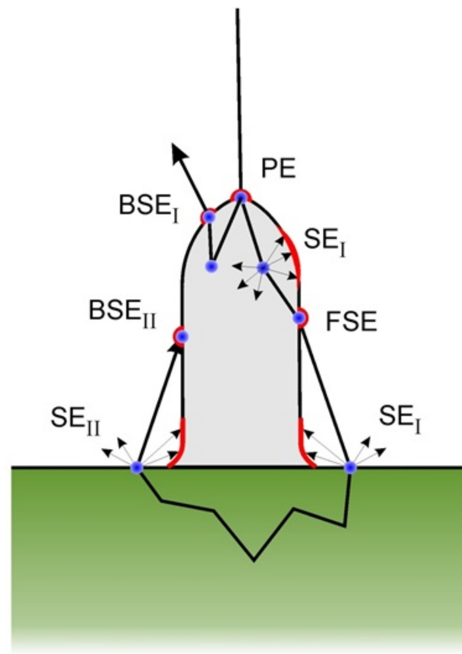

Figure 1.10: Schematic drawing of deposition events due to different electrons. [14]

electron beam, which is often reffered to as halo effect, which represents a fundamental limitation for the lateral resolution.

Gas flux and precursor migration

Besides electron beam properties and electron - molecule interactions, the supply of precursor gas molecules and their distribution on the substrate is of particular importance.

Since the deposition rate depends on the locally varying electron density as well as on the precursor molecule density on the relevant area, it is very important about the gas flux from the injection needle onto the surface. This distribution depends on the geometry of the gas injection system as well as on the gas flow itself. Figure 1.11 shows the geometry of the gas injection needle (a) as well as the distribution of the gas flow on the substrate (b) [12].

Since the deposition rate should be maximized, the molecule flux on the surface can be optimized by arranging the needle as close as possible to the surface. This can be obtained by a special geometries, such as shown in figure 1.12 [19].

As the electrons impinge on the substrate and dissociate some precursor molecules,

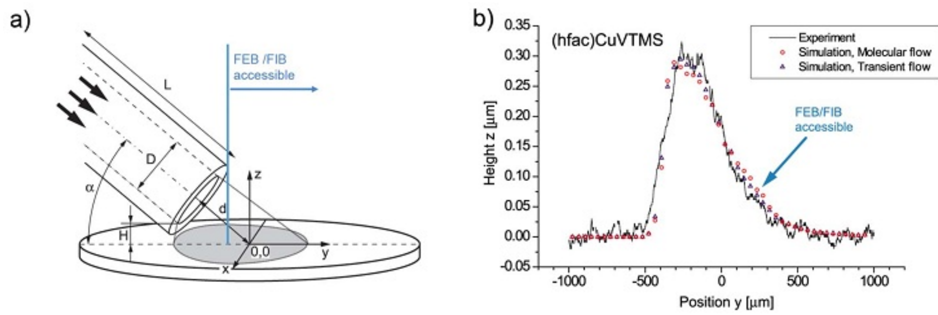

Figure 1.11: (a) Schematic drawing of the gas injection system geometry related to the surface. (b) Impinging precursor gas distribution with a tube inclination fo 60 and inner tube diameter of 0.5 mm. [12]

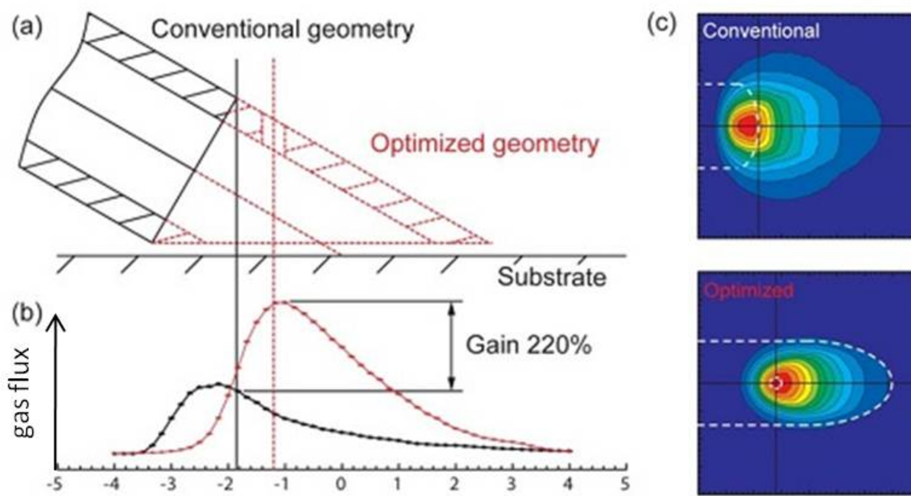

Figure 1.12: (a) Schematic drawing of the optimized gas injection system geometry. (b) Optimized molecule flux distribution in comparison with the flux of conventional shaped tubes. (c) Top view of molecule flux distribution. [19],modified

the area has to be replenished by molecule diffusion and by adsorption from the gas phase. Such replenishment processes require some refresh times depending on the beam depletion. So we get another important parameter, which is the time the electron beam spots one point (beam pulse duration) and is called dwell time. For longer dwell times the depletion of the local precursor is stronger, which requires longer refresh times for an appropriate replenishment. Figure 1.13 shows a top view of pillar rod pattern at different dwell times, but with identical total growth times. As one can see, small dwell times results in a high vertical growth rate, whereas long dwell times exhauste the precursor

molecule population during the beam pulse, which results in a smaller vertical growth rate. This behaviour can also be seen in figure 1.14. By further decreasing the dwell time the growth rate will also decrease due to some instrumental limitations, due to limited beam movement capabilities.

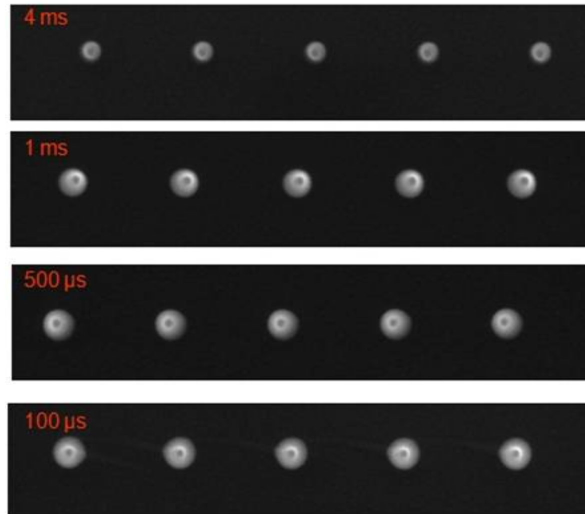

Figure 1.13: Single rod pattern with 500 nm spacing and different dwell times from 4 ms to 100 μs [14]

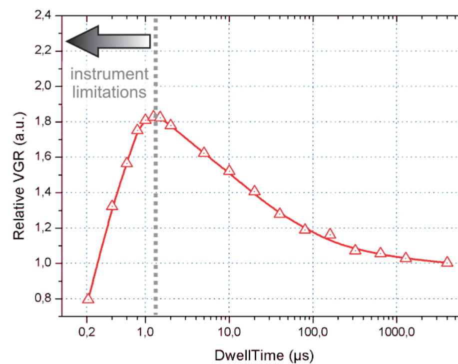

Figure 1.14: Volume growth rate dependency of the dwell time, revealing the instrumental limitations. [14]

Depending on the ratio between impinging electrons and available precursor molecules it is possible to divide into two regimes: 1) mass transport limited (**MTL**) regime, at which the deposition is limited by the providing of new precursor molecules; and 2) reaction rate limited (**RRL**) regime, for which a sufficient number of precursor molecules

is always available and the deposition rate is limited by the number of potentially dissociating electrons.

The MTL can further be divided in the diffusion assisted regime (**MTL-DA**) and the gas flux limited regime (**MTL-GL**). At MTL-DA the area where the electron beam impinges is assisted by diffusionn replenishment of new precursor molecules. This regime is shown in figure 1.15. Due to the growth of the structure, diffusion is getting more complicated for higher structures. As shown in figure 1.16 for some deposit height/geometry the diffusion based replenishment is negligible and the regime has changed entirely to MTL-GL regime condition. As discussed by these extreme cases it is obvious that the electron species - precursor molecule ratio is also a complex function influenced by geometric conditions during deposition. Starting from this height, the deposition is limited by the gas flux, which is resposible for reloading the sample surface.

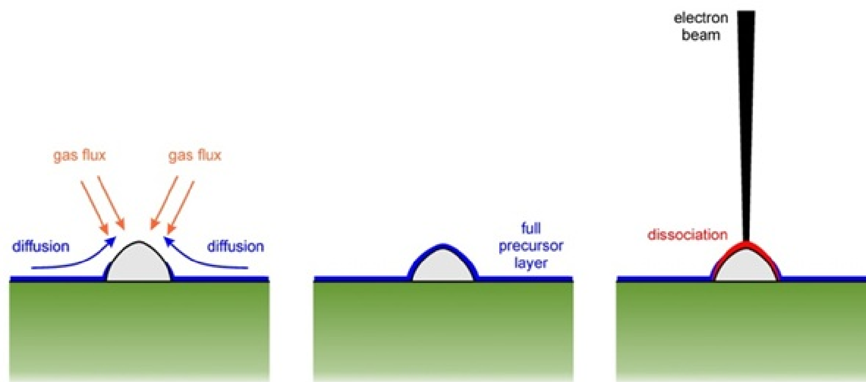

Figure 1.15: Schematics of diffusion limited regime.[14]

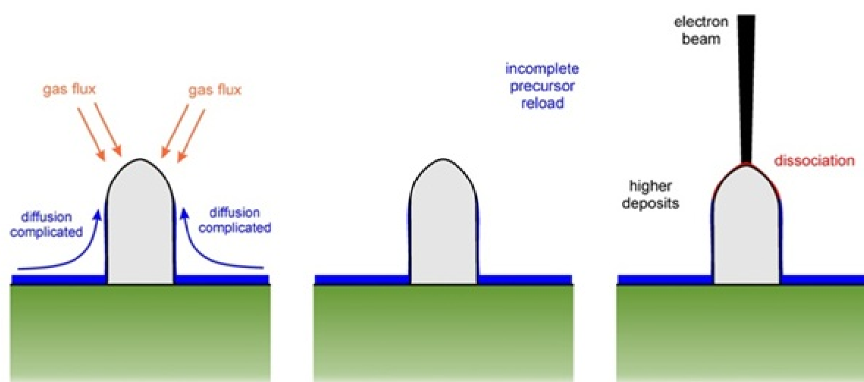

Figure 1.16: Schematics of gas flux limited regime.[14]

1.2 Atomic force microscopy

The atomic force microscopy (**AFM**) is a widely used method for surface characterization and manipulation at micro- and nanometer scale. Its biggest advantage compared to other surface characterization methods is, that AFM enables quantitative 3D surface mapping. Another advantage is the mostly effortless sample preparation and the widely non-destructive investigation methods, enabling further investigations.

Due to the implementation of many additional measuring techniques in recent years, it is possible to get further information beyond the morphology simultaneously, which can be correlated with the topography. Such methods allow for laterally resolved visualization of electrostatic, magnetic, chemical, resistance, etc. properties in correlation with the morphology [20], [21].

1.2.1 Components

The AFM uses a fine tip mounted on a cantilever as a sensor. This sensor is moved by a motion system established with a piezoelectric crystal. To measure fine cantilever deflections an optical laser detection system is used and these signals are analyzed in the controller.

Motion system

The motion system has to be capable of movements down to the Angstrom range. To meet such requirements motion systems are set up by piezoelectric elements, which are often combined to a tube scanner as swhown in figure 1.17 [22].

Applying a voltage to the concentric ring (Z)enables a vertical Z-movement by contracting or elongating the crystal. The X- and Y-direction movements are realized by applying a contrarious voltage to oposite cylinder segments which bend the crystal tube in the intended directions as shown in figure 1.17 (b).

Detection system

The detection system has to measure the cantilevers movements (deflection, torsion,...) with a high accuracy (sub-nm range) which is realized by an optical laser detection

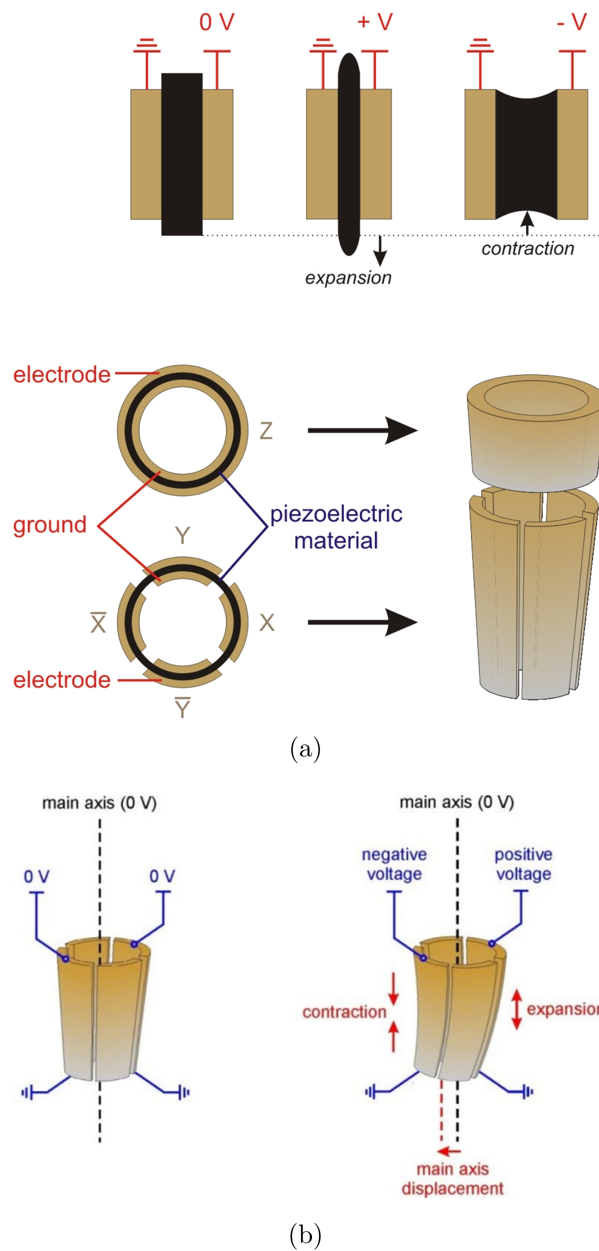

Figure 1.17: Schematic Design of a tube scanner. [14]

system. Such a system consists of a laser source, which focuses on the cantilevers end as shown in figure 1.18. The reflection is then focuses towards a position sensitive detector (**PSD**). When tip - sample interactions cause a deflection of the cantilever, which on his part shifts the laser reflection on the PSD as shown in figure 1.18 at the right.

Thus by changing the force on the cantilever, e.g. by morphological variations, the light path and so the position of the reflected laser spot changes on the PSD, which gives

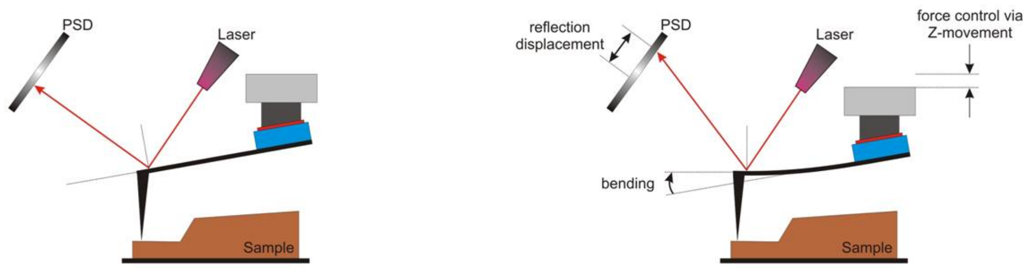

Figure 1.18: Schematic drawing of an optical laser detection system showing the light path at different scanner heights. [14]

therefore exact information of cantilever movement based on tip-sample interactions.

Cantilever and tip

As described before, the cantilever is an essential part of AFM, because its deflection is an indication for the probe - sample interaction. Because the cantilever deflection can be described by Hooke's Law $F = C_0 * x$, different cantilevers are classified by its spring constant. There are rectangular cantilevers with a relative high spring constant and triangular cantilevers with a smaller spring constant as listed in table 1.1.

	mode	length [μm]	spring constant [N/m]	resonance frequency [kHz]
Single Bar	tapping	160	≈ 42	≈ 360
Single Bar	tapping	240	≈ 2	≈ 70
Triangular	contact	100	≈ 0.02	≈ 10
Triangular	contact	200	≈ 0.6	≈ 70

Table 1.1: Typical properties of different tips used for different imaging modes(see section 1.2.2).

The geometry of the probe is critical for the quality of images. Figure 1.19 shows a commonly used tip. In order to take advantage of the highest resolution the probes apex has to be as sharp as possible, ideally delta-shaped. Typical commercially available tips show an apex radius of approximately 5-10 nm and a tip opening angle of approximately 30° with a pyramidal or tetragonal geometries [14].

Due to the non perfect geometry the AFM images must be considered as convolution

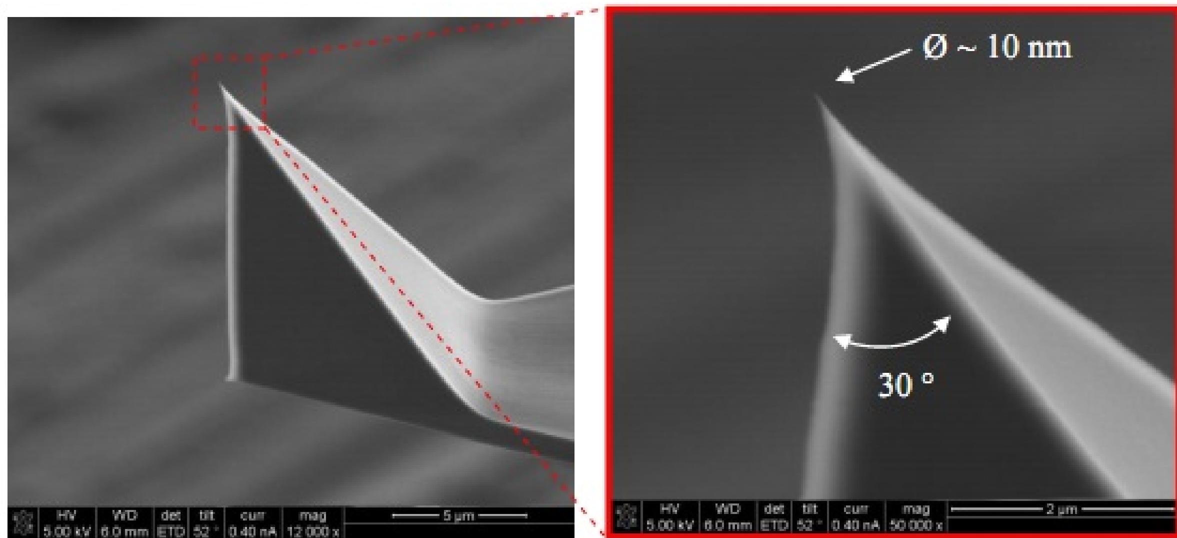

Figure 1.19: SEM picture of a tapping mode tip, showing the geometry. [14]

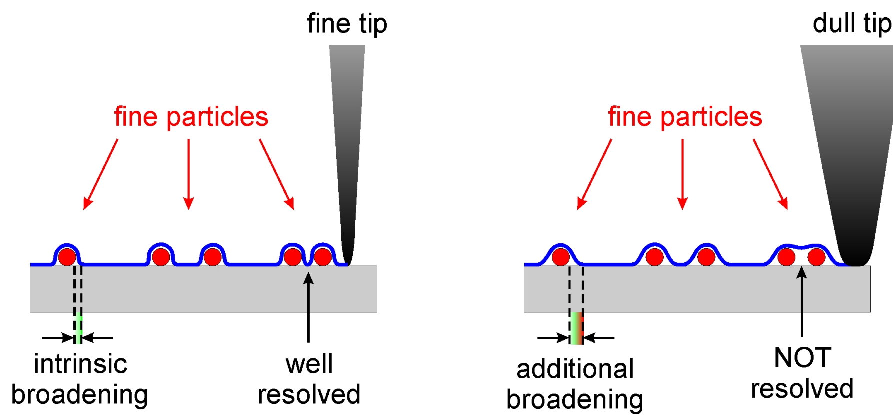

Figure 1.20: Comparison of line profiles with a fine and a dull tip. [14]

of the probe geometry and the sample surface. First of all the tip radius limits the lateral resolution, as shown in figure 1.20. Another important tip property is its opening angle, which affects in particular steep slopes, which can't be followed exactly due to the apex angle. Also the radial geometry influences the imaging process. Ideally the shape of the tip is rotationally symmetric to minimize this influence. As shown in figure 1.21, real structures get distorted due to the tip geometry.

For special measurements, such as conductive AFM (**C-AFM**), specially coated tips are commercially available. Such tips are more conductive than uncoated Si-tips, which is reqired for C-AFM measurements. However, they have also some disadvantages: 1) the apex radius is larger, because of the coating, so the maximum reachable resolution is

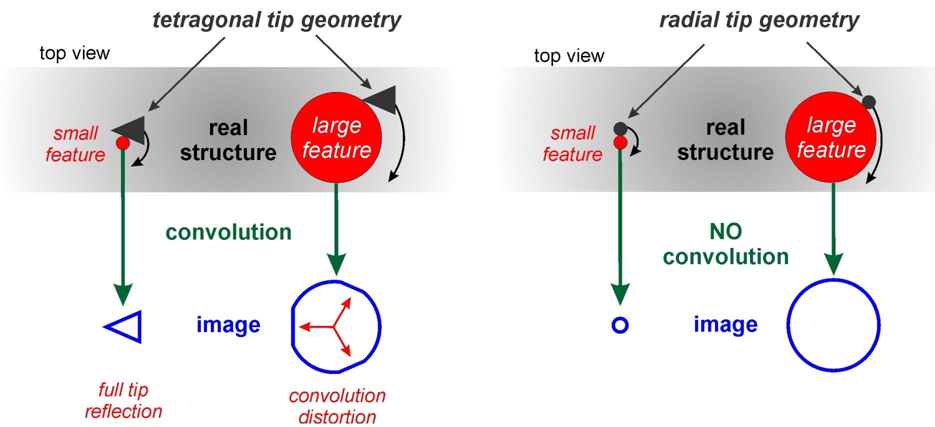

Figure 1.21: Convolution of tetragonal tip geometry in comparison with radial tip geometry. [14]

often decreased; 2) the coating may get damaged or partially removed by friction forces during scanning [23].

1.2.2 Topographical imaging

Imaging the topography requires a clear tip-sample interaction to entail cantilever deflections, which can be detected by the PSD. Dependent on the distance between the probe and the sample surface, there are different forces acting on the probe.

Distance r tip-sample	Type of interaction	Potential
> 10 nm	Electrostatic	$\frac{c}{r^2}$
10 nm - 0.5 nm	Van der Waals (dipole - dipole interaction)	$-\frac{a}{r^6}$
< 0.2 nm	e^- - e^- interaction (Pauli principle)	$\frac{b}{r^{12}}$

Table 1.2: Different forces acting between the tip and the surface at different distances

Typically the working distance is smaller than 10 nm, so the electrostatic force can be widely neglected and the interaction can be described by the Lennard-Jones potential

(blue line in figure 1.22) according to:

$$V_{LJ} = V_{rep} + V_{VdW} = \frac{b}{r^{12}} - \frac{a}{r^{6}} \quad (1.4)$$

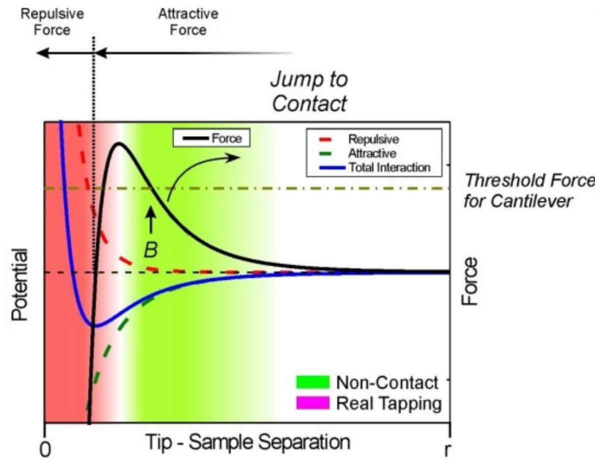

Figure 1.22: Lennard-Jones potential and actual force acting to describe the interaction between tip and surface. [14]

By differentiating equation 1.4 one can get the actual force acting on the probe. With the help of this force one can divide the tip - sample interactions into an attractive and a repulsive regime (green respectively red areas in figure 1.22). By approaching the surface, the tip firstly gets slightly bend down because of the attracting force, followed by a change into repulsive forces, as the distance is lowered, which bends the cantilever slightly upwards.

For the image formation it is important to approach the tip to the surface to a point, where a clear force acts on the tip. The cantilever will get deflected in a certain position, which is detected by the laser reflection on the PSD. In the next step the motion system moves the tip along the x-direction and depending on the morphology, the cantilever deflection changes which is detected by the PSD. The motion system regulates now the vertical scanner position in such a way, that the laser reflection will end up in the same position as for the previous point on the surface, ensuring same forces between surface and tip on both positions. The vertical Z-position of the scanner for every point X,Y can be interpreted as topography image.

Contact Mode

In contact mode, the cantilever deflection due to repulsive forces is kept constant. As described before, this is enables via vertical displacement of the scanner, which provides 3D topography information.

The big advantage of contact mode is the comparable high scan rate and the atomic resolution capabilities for adequate materials, like mica or graphite [14]. On the other hand the direct tip to surface contact can cause some problems. First of all, soft samples can be damaged by the hard tip by some material removment or scratching, but also some particles can be attached from the sample to the tip, so the image will be afflicted by artefacts as shown in figure 1.23.

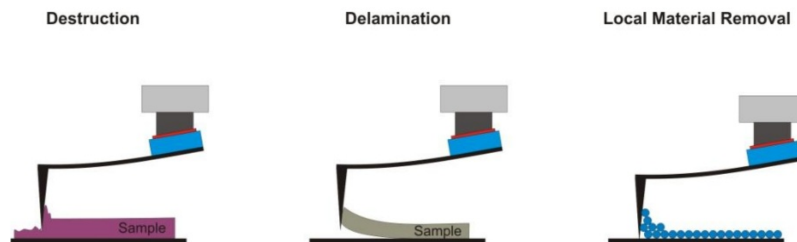

Figure 1.23: Schematic drawing of possible damage caused by direct tip - sample contact [14].

Tapping Mode

In order reduce the direct contact of the probe with the sample, the cantilever is oscillated at its intrinsic resonance frequency, mechanically excited by another piezoelectric crystal, as shown in figure 1.24. The result is an oscillating tip, which taps the surface, which reduces the time of mechanical contact. Instead of a laser displacement at the PSD caused by cantilever deflection in contact mode, in tapping mode the average amplitude (**RMS** amplitude) is used as control signal.

By approaching the probe to the surface the amplitude of the oscillation is damped due to the tip-sample interactions [20]. This damping is a convolution of energy dissipation by the partially contact and a shift of the resonance frequency through tip-sample coupling. As the tip-sample interaction affects the resonance frequency and the cantilever is excited with a constant force, the result is a reduced amplitude, as shown in figure 1.25. This damped amplitude is detected by the PSD and used in the same manner to

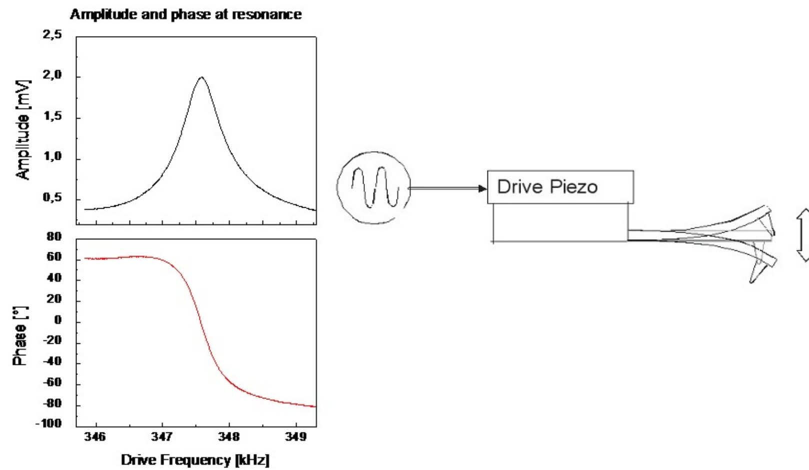

Figure 1.24: Schematic drawing of the excitation of the cantilever by a piezoelectric crystal. Also shown amplitude and phase of a tip at resonance frequency depending on the drive frequency. [20], [24]

keep the amplitude constant for each point X,Y.

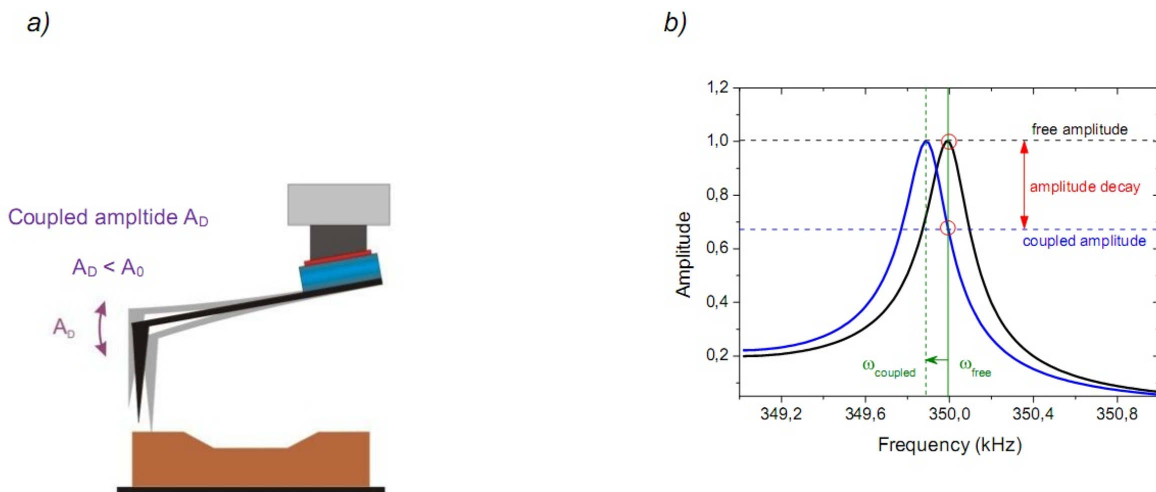

Figure 1.25: (a) Schematic drawing of approached tip, (b) plot to visualise the amplitude damping caused by attractive tip-sample interaction [14].

In this tapping mode the working regime can be selected in conjunction with the phase lag signal between excitation and response oscillation described in detail in Ref [Skript AFM Harald] by choosing the parameters. Firstly there is the non-contact regime, where the probe doesn't get in physical contact with the surface due to the exclusive attractive tip-sample interactions. This regime is very important, when the surface should not be touched for some reasons. The other regime is the intermittent regime, where the probe

taps the surface, in which repulsive forces are predominant, which can be of advantage for adhesive samples [21], [24].

1.2.3 Kelvin Probe force microscopy

For electrostatic measurements Kelvin probe force microscopy (**KPFM**) is a widely used method, which is capable of measuring the contact potential difference (**CPD**) between the probe and the surface [25], [26], according to, where ϕ_{tip} and ϕ_{sample} are the working functions of the tip respectively the sample:

$$V_{CPD} = \frac{\phi_{tip} - \phi_{sample}}{-e}. \tag{1.5}$$

In our system, KPFM is a two-pass technique: during the first pass the topography is measured in tapping mode, where the cantilever is excited mechanically. On the second pass the tip is set to a lift height, where it follows the line profile measured in the first pass. During this pass the cantilever is only excited electrically at its intrinsic resonance frequency with a voltage according to:

$$V_{tip} = V_{DC} + V_{AC}\sin(\omega t) \tag{1.6}$$

With V_{DC} the applied DC voltage, V_{AC} the applied AC voltage and ω the resonance frequency of the cantilever. By approaching an electrically conductive tip to the surface, an electrostatic force is generated due to the different fermi energy levels. This electrostatic force is given by:

$$F_{es}(z) = -\frac{1}{2}\Delta V^2 \frac{dC(z)}{dz}. \tag{1.7}$$

Here z is the direction normal to the sample surface and ΔV is the potential difference between the voltage applied to the tip and V_{CDP}.

$$\Delta V = V_{tip} \pm V_{CPD} = (V_{DC} \pm V_{CPD}) + V_{AC}\sin(\omega T) \tag{1.8}$$

By inserting ΔV into equation 1.7 one gets three parts:

$$F_{es}(z) = F_{DC} + F_{\omega} + F_{2\omega} \tag{1.9}$$

$$F_{DC} = -\frac{\partial C(z)}{\partial z}[\frac{1}{2}(V_{DC} \pm V_{CPD})^2] \tag{1.10a}$$

$$F_{\omega} = -\frac{\partial C(z)}{\partial z}(V_{DC} \pm V_{CPD})V_{AC}\sin(\omega t) \tag{1.10b}$$

$$F_{2\omega} = -\frac{\partial C(z)}{\partial z}\frac{1}{4}V_{AC}^2[\cos(2\omega t) - 1]. \tag{1.10c}$$

Equation 1.10a isn't used for measuring V_{CPD}, because it describes a static but very small deflection of the AFM tip. With equation 1.10b the actual V_{CPD} is measured. As one can see, a force F_{ω} is arising if $V_{DC} \neq V_{CPD}$. Due to the sine modulation at ω, Fω oscilates the cantilever at its resonance frequency, which can be detected by the PSD. By applying an accurate voltage V_{DC} to the AFM tip force will be zero and so the measured amplitude nullifies for $V_{DC} = V_{CPD}$. This value V_{DC} is adjusted for each point individually, which yields a laterally resolved map of the surface potential. The different cases can be seen in figure 1.26. Equation 1.10c is usefull for controlling the applied voltage, due to the fact, that it is the derivative of 1.10b and for a small voltage change it is used to verify in which direction the voltage has to be changed [27].

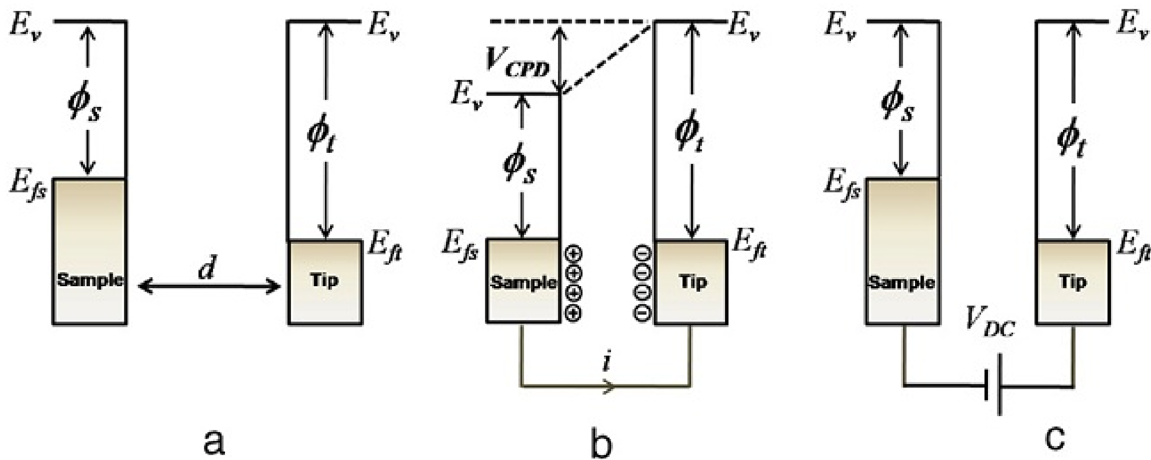

Figure 1.26: Energy levels of AFM tip and sample. (a) no electrical contact due to separation by distance d, (b) electrical contact, (c) applied external bias V_{DC} between tip and surface to nullify CPD. [27]

There are also some challanges for this method. First of all, the most important parameter affecting reliability of KPFM, is the tip-sample separation. In KPFM mode the signal is convoluted by contributions of the cantilever, the cone and the apex, whereupon only the contribution of the apex is desired. The other contributions are highly undesired, due to limiting the lateral resolution and displacing the measured signal. Figure 1.27 shows the different contributions in dependency on sample - tip distances.

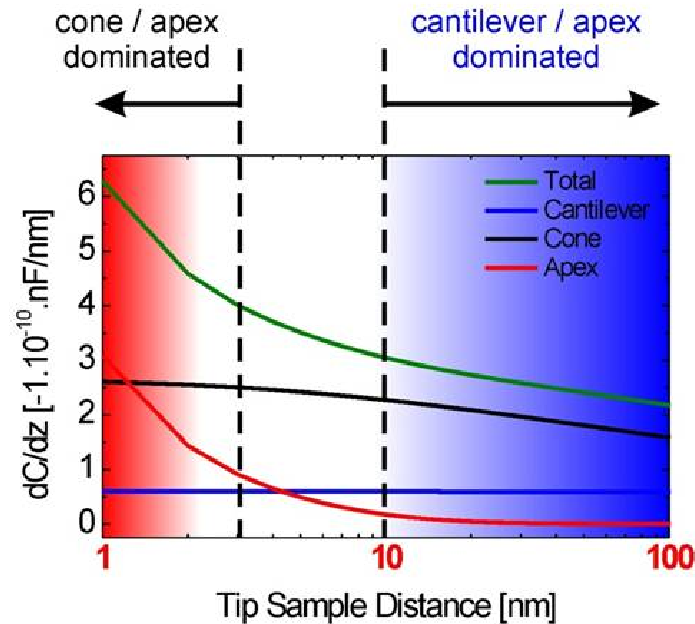

Figure 1.27: Illustration to show how the individual parts of the cantilever conrtibute to KPFM signals. [14]

At large distance, the cantilever primarily interacts with the sample. However, reducing the tip-sample distance down to a few nm the tip apex interaction gets dominant, although the measured value remains still a convolution of all the components. Because of this convolution the real potential is always higher than the measured one, which makes absolute measurement without a standard practically impossible. Hence, the resolution depends on the tip - sample distance and the maximal lateral resolution of ≈ 20 nm will be reached at the tip apex dominated distances of a few nm [27].

1.2.4 Conductive AFM

At conductive atomic force microscopy (**C-AFM**) an electrically conductive probescans the surface in contact mode. Simultaneously to the topographic image the current between the sample and tip is recorded, which provides a laterally resolved current image. So for C-AFM measurements the conventional AFM has to be extended by a conductive AFM probe, an external voltage source, a current amplifier and a current-voltage converter (**CVC**). The current amplifier has to be highly sensitive, because at hight resistance samples the measured currents can be down to a few femto- or picoamperes. The external voltage source is required to apply a voltage between the tip and the sample to enable a current to flow and get the desired information. In our system the voltage can vary between the range of ± 12 V, which however, can be expanded up to 230 V.

Perhaps the most important fact that has to be taken into account is the choise of the probe for C-AFM measurements. In principle any conductive AFM probe, e.g. conventional doped silicon probes, can be used. With such probes the problem of damaged coatings may be solved, but on the other hand the electrical properties are considerably improved with coated tips. E.g. commercially available are conventional contact mode tips with following coatings: heavily doped diamond, PtIr, TiN, W_2C, and Au, but also probes, which are made entirely out of diamond are available.

Coating	**Pt**	**Au**	**W_2C**	**PtIr**	**Diamond**	**TiN**
Work function [eV]	5.65	5.10	3.8	5.6	5.7	4.8-5.3

Table 1.3: Summary of work functions of different conductive coatings of AFM tips. [23]

The choice of tip is always some kind of compromise between the probe life time and the desired resolution. For example, PtIr or Au coated tips have a rather low resistivity of 0.01 - 0.025 Ωcm compared to diamond coated tips with 0.5 - 1 Ωcm, but due to their soft coatings, their lifetime is lower. In addition the metal coated tips have a apex radius of approximately 35 nm, whereas diamond coated tips can have a radius of more than 100 nm. Another issue by choosing the tip is the work function of the different coatings, which has influence on the tip-sample electrical contact and barrier height [23].

1.3 Experimental details

1.3.1 Electron beam induced deposition - details

For the structure production a SEM/FIB dual beam microscope was used, combining an electron with a focused ion beam microscope. The electron source in this microscope is an field emission gun (**FEG**), is capable of electron energies in the range of 1 - 30 keV, with currents ranging from 2.5 up to 37,000 pA resulting in beam diameters down to 1.2 nm (FWHM).

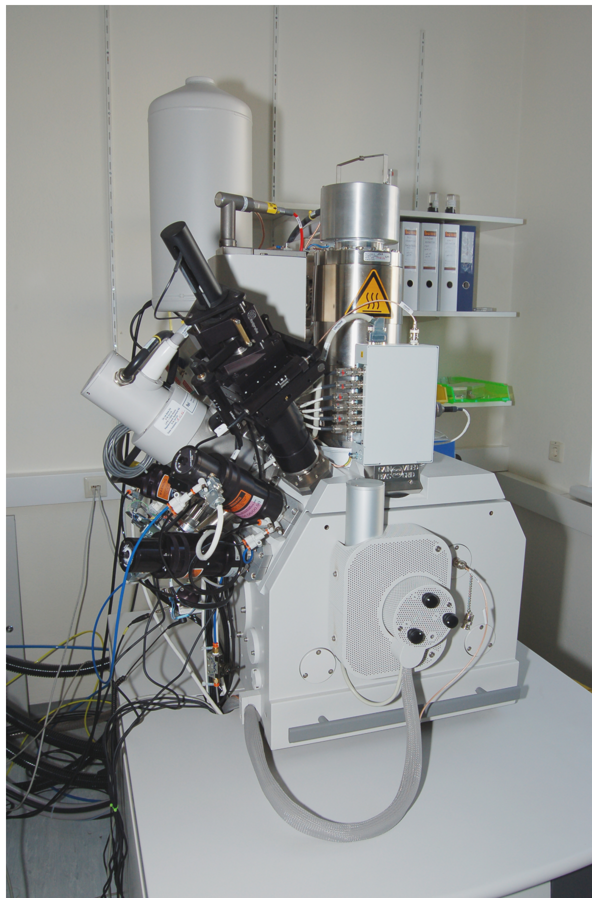

Figure 1.28: Used SEM/FIB Dual Beam Microscope (FEI Nova 200 Nanolab).

As substrate, 1x1 cm^2 pieces of a B doped Si-Wafer were used, covered with a 3 nm SiO_2 layer revealing roughness of approximately 0.1 nm (RMS).

Used precursor gas

As precursor gas Trimethyl-methylcyclopentadienyl-platinum ($MePtCpMe_3$) was used. The chemical structure is shown in figure 1.29, while table 1.4 summarizes the physical properties. In figure 1.30 an ideally dissociated precursor molecule with its individual fragments is shown.

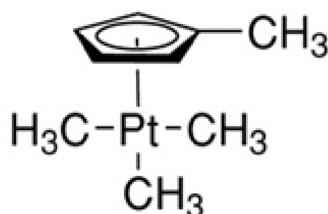

Figure 1.29: Chemical formula of Trimethyl-methylcyclopentadienyl-platinum.

Color and Form	off-white powder
Molecular weight	319.32
Melting point	30-31°C
Boiling point	23°C @ 0.053 Torr
Vapour pressure	0.2 Torr @ 35°C,0.053 Torr
Specific gravity	1.88
Odor	metallic
Solubility in water	insoluble

Table 1.4: Properties of Trimethyl-methylcyclopentadienyl-platinum. [3]

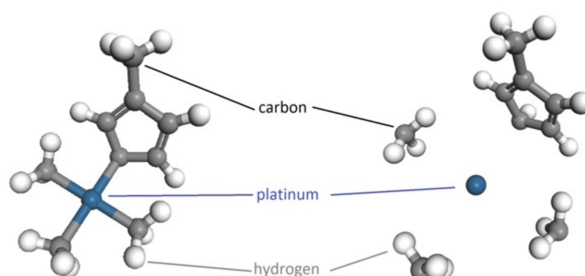

Figure 1.30: Used precursor on the left side and cracked precursor fragments on the right side. [3]

One problem with this precursor molecule is, that full dissociation is not a single electron based event [28], [29]. As a result, the Pt deposits are not 100 % Pt but consists

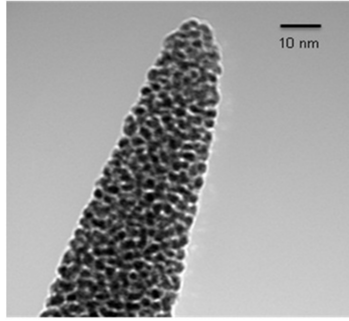

Figure 1.31: Bright field TEM image of a deposited nanorod showing the Pt-crystals embedded in a carbon matrix. [9]

of small Pt crystals ($\approx$ 1.7 nm) embedded in a carbon matrix. This composition has typically 15 at.% metal content. Figure 1.31 shows a nanorod deposited with EBID and one can easily see the inhomogeneous deposition. The dark parts in this bright fiel TEM image are the Pt-crystals, which are embedded in the carbon matrix, which is the bright part in the TEM image.

As mentioned above one electron interaction event is unlikely to crack the complete precursor molecule. Due to this dissociation into a compound instead of pure platinum, the electrical conductivity can be reduced or hindered due to an electrical resistivity by 5-6 orders of magnitude higher than pure Pt. Therefore, high volumes must be deposited to achieve acceptable conductivity, which comes into conflict with the deposition of conductive nanostructures. A solution for this problem is the improvement of conductivity by post growth purification, which leads to an improved conductivity by at least 3 orders of magnitude [3], [30]. The second approach is the definition of design rules for the deposition, which is the intention of this thesis and will be discussed further.

Structure Deposition

$1 \times 1\ \mu m^2$ structures were fabricated with heights ranging from less than 10 nm up to approximately 100 nm. The acceleration voltage is varied from 5 to 30 keV in 5 keV steps.

The electron beam, which is dissociating the precursor gas, is not moved continuously, but in discrete steps called pulsed deposition. As discussed in section 1.1.2, the beam is hold on one position for the dwell time. The dwell time is chosen to be 100 μs for all our structures, to prevent strong local depletion on the one hand and as a consequence the

introduction of long refresh times on the other hand. These single points are scanned from left to right for each line, as shown in figure 1.32.

1	2	3	4	5
6	7	8	9	10
11	12	13	14	15
16	17	18	19	20
21	22	23	24	25

Figure 1.32: Image for illustration of deposition points scanned periodically line by line. [3]

As the electron beam runs through such a cycle, one loop is completed. The loop number is then used for the deposit height control and an essential parameter for the height design rules. After completing one loop the beam is moved to a synchronisation position apart from the pattern, which is, howeber, highly unwanted for AFM measurements. To avoid this position to be on the designed structures itself stream files have been generated as shown figure 1.33. On the top left corner the 1×1 μm^2 deposit is structured and on the bottom right corner, there is one point used for synchronisation with a dwell time of 10 μs.

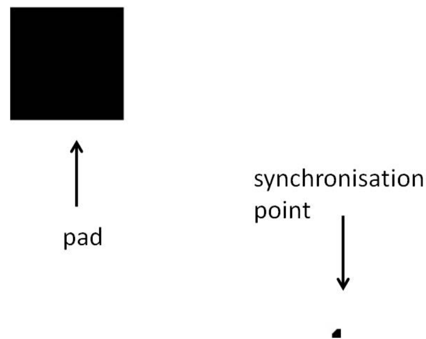

Figure 1.33: Illustration of stream file designed for structure patterning.

The used parameters for the different acceleration voltages are summarized in table 1.5.

For relocating the structures in the AFM a marker is drawn on the top left corner of the substrate and a coordinate system with its origin on the marker is set onto the

acceleration voltage [keV]	**dwell time** [μm]	**beam current** [pA]	**point pitch** [nm]
5	100	98	14.9
10	100	130	11.58
15	100	140	9.69
20	100	150	8.6
25	100	150	7.75
30	100	150	7

Table 1.5: Summary of used parameters for different acceleration voltages.

sample, so the +X-Axis is from the vertical edge to the right and the -Y-Axis is from the horizontal edge down. Figure 1.34 shows where the different structures are deposited[1].

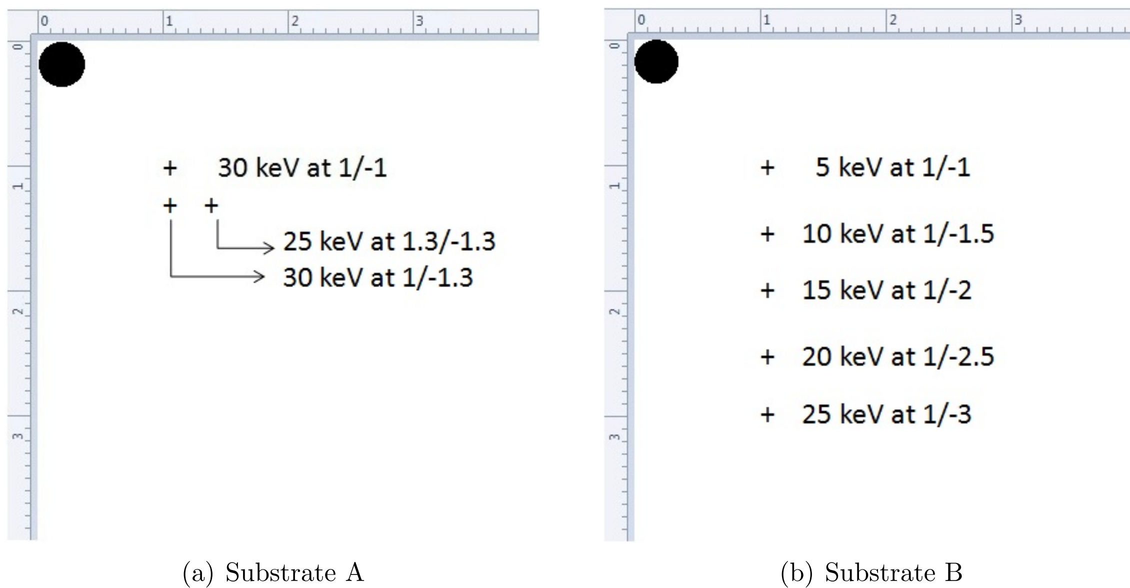

(a) Substrate A

(b) Substrate B

Figure 1.34: Drawing of the alignment of the particular structures on the two substrates. On the top left corner a marker is drawn on the substrate.

In figure 1.35 the arrays for the different acceleration voltages are shown. For every particular voltage and loop number, 3 or 4 structures are made to ensure the quality of analysis. Between the structures one has to navigate "‘blindly"’ in the SEM to prevent electron beam induced carbon contamination of the sample surface. The additional structures are made with 100 and 150 loops for 30 keV and 200 and 300 loops for 25 keV. The structures marked grey are designed with some wrong parameter and therefore not used for analysis.

[1]all distances in mm

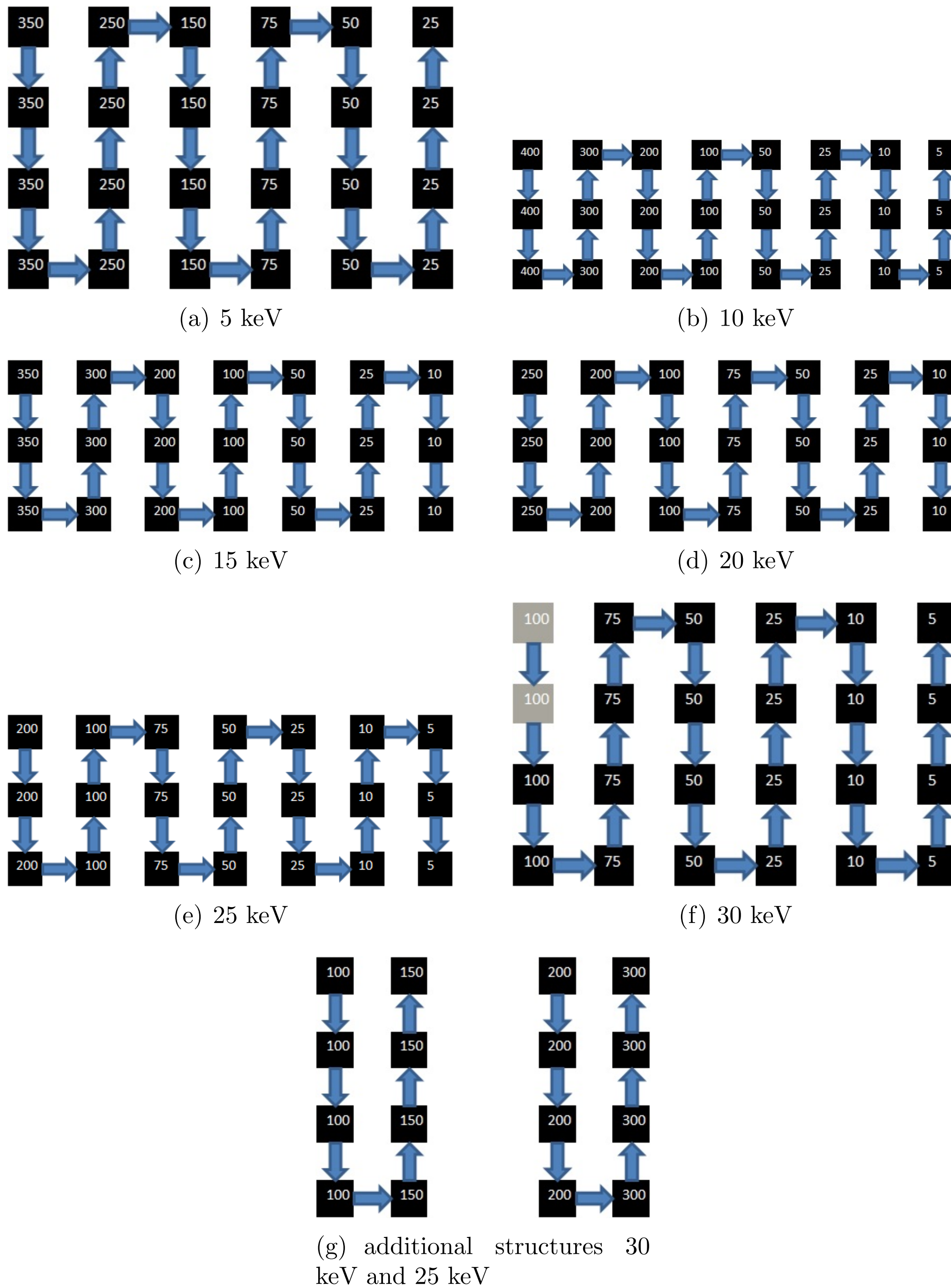

(a) 5 keV (b) 10 keV

(c) 15 keV (d) 20 keV

(e) 25 keV (f) 30 keV

(g) additional structures 30 keV and 25 keV

Figure 1.35: Alignment of the structures for the particular acceleration voltages. Grey structures are designed with some wrong parameter.

The structures for conductivity measurement via C-AFM were deposited on a conductive Au path. Therefore, the conductive supply conductor of a damaged four point structure was taken. The first pattern was structured with 30 keV and a dimension of

$4\times1\mu$m, as shown in figure 1.36.

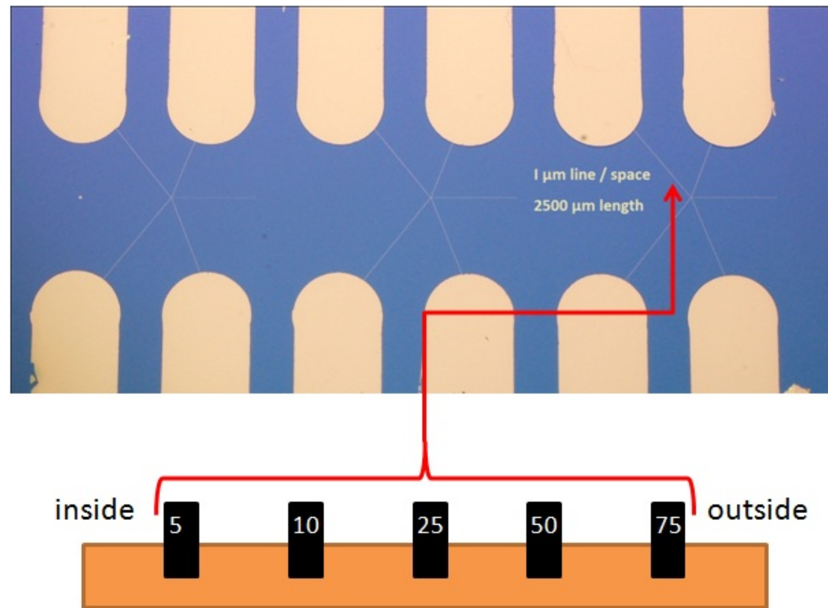

Figure 1.36: Schematic drawing of the alignment of 30 keV structures on conductive path.

1.3.2 Atomic force microscopy - details

For AFM investigations a Dimension 3100 System from Bruker AXS[2] was used (see figure 1.37). This AFM is placed on an active vibration isolation plate, to minimize mechanical vibrations. The whole system is placed in a glove box operated with nitrogen, to get an inert atmosphere and reduce the hydrogen adsorption on the sample surface. This AFM is equipped with an Nanoscope IV controller, which is placed in the room next to the glove box to avoid acousitc vibration influences.

For analyzing the captured files "NanoScope Analysis v1.20"[3] was used. With this software the images obtained from scanning the structures were reprocessed by flattening and plane fittting for getting proper quality images. For the investigation of the radius of the outer and inner halo, the x-y curves of sections on the structures of the height and KPFM line scans were exported from this software and imported in Origin.

Due to working with KPFM, which requires interleave mode, the image resolution is

[2]former Veeco Instruments
[3]Bruker AXS

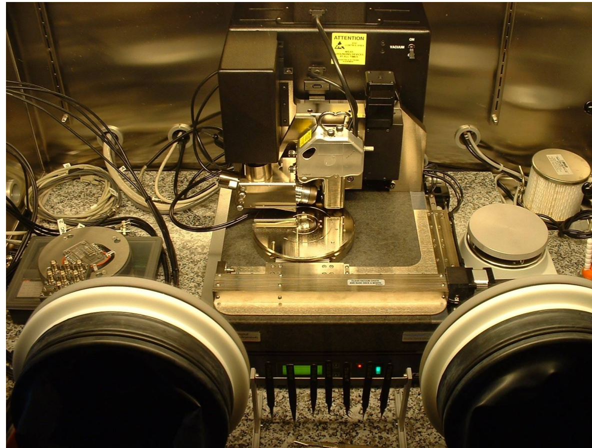

Figure 1.37: Used atomic force microscope, placed on isolation plate.

limited by 512 pixels and lines, because the system isn't able to capture the maximal resolution of 1024 pixels for both, main and interleave scan.

There are some different types of tips, which were used during this diploma thesis. Due to the early stage of C-AFM experience, some different tips were used to evaluate this method, its requirements and the reliability. Their properties are summarized in table 1.6

- **Olympus tapping tips (OMCL-AC240-TS)[4]:** Due to KPFM measurements and the available controller of the AFM, one is limited to use tips with a resonance frequency below approximately 120 kHz. These tips were also used for C-AFM measurements.
- **PtIr coated tips (SCM-PIT) [5]** for C-AFM measurements. There were two types of PtIr coated tips with different cantilever length, resulting in different resonance frequencies and spring constants.
- **TiIr coated tips (ASYELEC-01)[6]** also for C-AFM measurements. Due to some problems, such as particle contamination of the probe, scratching onto the sample or surface abrasion, one has to reduce the force between the probe and the sample. This can be done with a longer cantilever, resulting in a smaller spring constant. Also the different coating can turn the contamination of the probe for the better.
- **New type of Olympus tapping tips (OMCL-AC240-TS):** Because the Olym-

[4] [http://www.atomicforce.de/Olympus-Cantilever-Tip-Properties-ac240ts.php]
[5] [www.veecoprobes.com]
[6] [www.AsylumResearch.com/Probestore]

pus tapping tips were short in supply, a new charge of uncoated tips was ordered. These cantilevers have a changed geometry, but their properties remain unchanged.

	resonance frequency [kHz]	**spring constant** [N/m]	**cantilever length** [μm]	**tip radius** [nm]
OMCL-AC240-TS	≈ 70	≈ 2	240	< 10
PtIr coated tips	≈ 70	≈ 3	240	≈ 25
PtIr coated tips	≈ 120	≈ 3	120	≈ 25
TiIr coated tips	≈ 70	≈ 2	240	≈ 23
uncoated Si tips	≈ 70	≈ 2	240	< 10

Table 1.6: Summary of properties of used tips.

After inserting the tip into the tip holder and mounting the holder onto the scan head, the laser beam has to be placed as close as possible to the front of the cantilever to get a minimized cantilever oscillation with the same signal strengh on the PSD. This minimized amplitude will ensure a minimized risk of sample damage [24]. So when the laser beam is positioned accurately, the Auto Tune process has to be run. This process will adjust the excitation frequency with the resonance frequency of the cantilever. This firstly has to be done for tapping mode measurements for the mechanical excitation, but also for contact mode measurements it is advised to be done, for ensuring that the laser beam is positioned correctly.

Topography and KPFM measurements

After setting up the cantilever and laser beam accurately, one can approach the tip to the surface. For KPFM measurements it is very important not to touch the surface at any time to prevent sample and tip damage. Hence, before activating the interleave mode to measure the contact potential difference, stable non-contact conditions has to be established, which must be done by using the phase signal (more details can be found in [21], [25], [26]). Then the interleave mode is activated with a starting lift height of ≈ 50 nm. This lift height is reduced as long as the sample surface isn't touched by the probe, but the probe is within 5 nm surface - probe distance. For ensuring this the potential signal has to be observed carefully, which will change rapidly by getting closer than ≈ 2 nm. Observing this change in the potential signal the lift height is increased again about 2 - 5 nm to ensure a stable signal without interference edges. By this process one can assure to be in a regime, where the tip instead of the cantilever is dominating

the contact potential measurement. This will ensure comparable results for successive measured structures.

C-AFM measurements

For the C-AFM measurements, the gold pads, shown in figure 1.36, have to be contacted to apply a voltage between the conductive Au - path and the probe. To set this up an active sample holder was used, shown in figure 1.38.

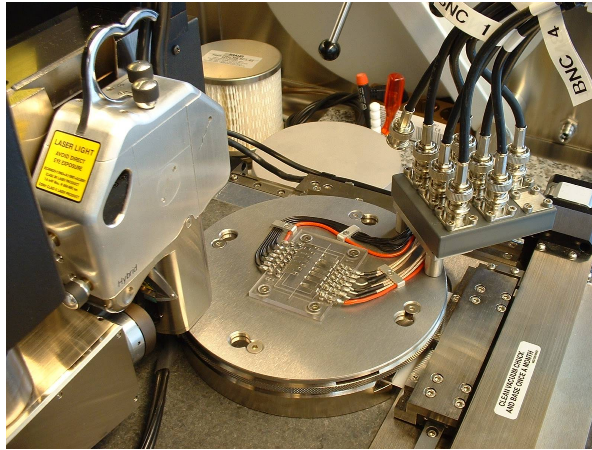

Figure 1.38: Active sample holder for contacting the Au - pads to apply a voltage between the tip and the sample surface.

To get the voltage applied to the conductive path the active sample holder has to be connected to the signal access box (**SAB**) by some coaxial wires. The Au - pad that has to be applied to the voltage has to be connected to the Analog 2 channel, where one can control the voltage on the software. The Au - pad on the opposite side has to be connected to ground, because otherwise the measurement will be disturbed.

After setting up the active sample holder and installing the tip onto the scan head, the laser beam has to be adjusted. Due to working in contact mode, while measuring the current, the laser beam has to be set up so that the reflection comes on the PSD at a vertical displacement of 0 V and a horizontal displacement of ≈ 2 - 3 V. In this diploma thesis a value of ≈ 2.8 V was set up for all C-AFM measurements, for getting comparable forces acting between the probe and the sample. The deflection setpoint is set to - 2.3 V for the engaging process to minimize the force on the sample and thus minimizing the risk of damaging the sample. Due to the quality of the topography image one has to adjust this deflection setpoint and hence increase the force between the probe

Figure 1.39: Signal access box to plug in the coaxial wires for applying some voltage to the active sample holder.

and sample, which increases the risk of damage as well.

The voltage applied on the conductive path can be arranged between ± 12 V via the software. Due to some losses the maximum real voltage applied is ≈ ± 11 V. Further values are the adjustments taken on the software and not the real voltage applied on the sample.

1.3.3 Simulations

To get an insight of the electron trajectories within the deposited structure and the substrate, simulations have been performed with Software CASINO [7] v2.42 [31] .

With this programm one can simulate electrons impinging a surface ranging from 0.1 up to 30 keV and calculate their trajectory in the solid of your choise for multi-layer samples and also grain boundaries. Usually it was programmed for predicting SEM signals, but we use it as tool for estimating the radius of the backscattered electrons as a first prediction for the outer halo. For this simulations a multi-layer geometry with a Si-substrate and a 3 nm SiO_2 layer on top was used. For simulating the electron source 2,000,000 electrons were calculated with an electron beam radius of 2 nm.

Further simulations considered the number of points contributing to the forward scattering and thus to unwanted additional deposition. These simulations were also done with a multi-layer geometry with a 100 nm Ti-layer, which shows a resulting Z identical

[7]acronym for Monte ”‘**CA**rlo **SI**mulation of electro**N** trajectory in s**O**lids”’

to a typical Pt/C atomic ratio of 15/85, on top, but with no substrate under the Ti-layer. This will prevent electrons from being backscattered from deeper Ti-areas than 100 nm and thus distort the width of electron scattering. Because these simulations only have to show the trajectories of penetrating electrons and no distribution of backscattered electrons or some energy distribution was calculated, only 5,000 electrons were simulated and displayed.

2 Results

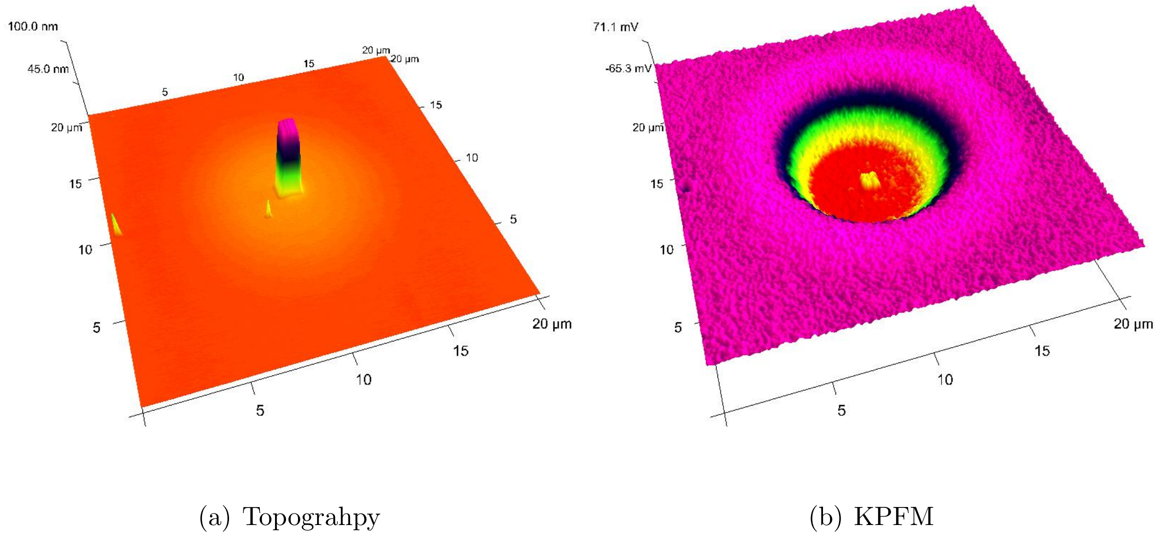

(a) Topograhpy

(b) KPFM

Figure 2.1: Height (a) and KPFM (b) image of an electron beam induced Pt deposit revealing the unwanted halo.

Extensive experiments revealed unwanted halo effects around the intended Pt deposits, as shown in figure 2.1 by a correlated height (a) and potential (b) image with same dimensions. One can see the additional halo in the topography image (a) as a light orange halo and in the surface potential image (b) as a severe changing from purple to red. However, detailed analysis revealed three different effects, as systematically shown in figure 2.2: first of all, there is an outer halo $\mathbf{H}_o$, which shows a typical radius of a few micrometer for 30 keV, secondly there is an edge halo $\mathbf{H}_{edge}$ found, which broadens the structures side walls to some trapezoidal instead of rectangular cross sectional geometry. The third effect is the inner halo H_i, which describes the halo formed by the forward scattered electrons, which is inbetween the dimension of the H_{edge} and H_o. All three appear in different shapes for different deposition parameters, such as the electron energy.

The main dependency, however, is found for the primary electron energy (acceleration voltage), which leads to our concept, in which we propose that 1) the outer halo is formed by the BSE reemitted from the substrate and 2) the inner halo is generated by FSE emitted from the deposit side wall and 3) the edge halo is formed by additional secondary electron deposition. Figure 2.2 shows a schematic drawing of typically found cross section in which the different halo types are indicated.

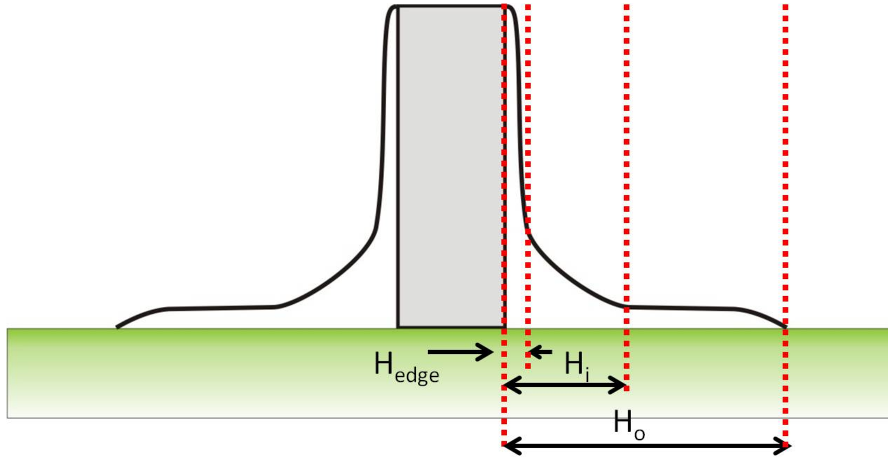

Figure 2.2: Schematic classification of deposited structures showing the inner, the outerand the edge halo.

The main aim of this thesis is the determination of the resolution limitating factor for fabricating Pt - structures and the separation of technical and design related from intrinsic limitations. Whereas the design related limitations are tunable, the intrinsic limitations are not. This knowledge allows for specific change in deposition parameters to achieve lowest proximity deposition. To achieve this, we started with the investigations on the 30 keV structures as a representative characterisation of all effects. Futhermore we took a look at the energy and height dependent evolution of the different halos, conluding with a comparison of the different effects.

2.1 Representative characterisation of halo effects

First of all a function was calculated, which describes the height dependency on the loop number for further designing defined deposit heights to provide comparability for different energies. To find this function the heights derived from AFM measurements are plotted vs. the loop number and fitted linearly in Origin, as shown in figure 2.3. For the given deposition parameters, as listed in table 1.5, the following function is obtained, with the height h and the loop number l:

$$h = 0.36 \cdot l \tag{2.1}$$

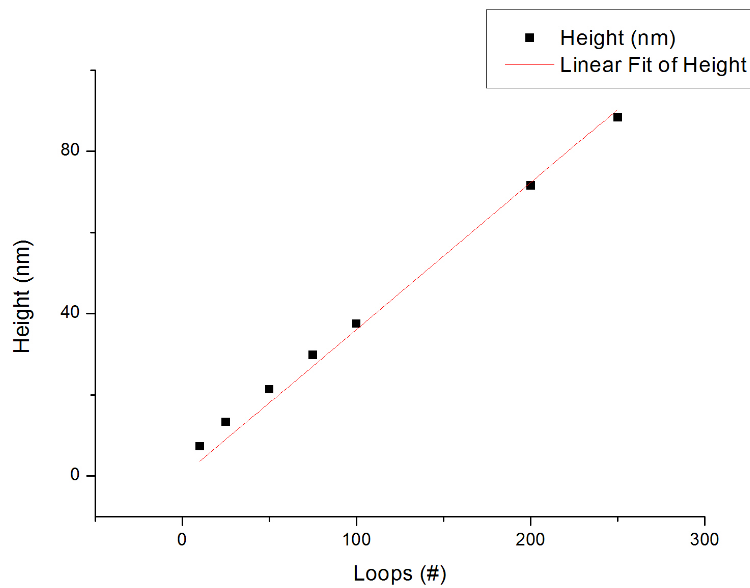

Figure 2.3: Height measurements of the fabricated structures plotted in dependency on the loop number and linearily fitted with an intercept of zero.

For finding the radius of the inner and outer halo, individual cross section profiles derived from AFM and KPFM measurements have been analyzed. As one can see in figure 2.4, the radius of the outer halo H_o ranges from the edge of the structure to the last distinguishable variance of the flat substrate. The edge halo H_{edge} radius ranges from the same inner edge to the first change in the curvature of the structure's slope. The inner halo H_i is defined from the inner edge to the variance of the H_o. For defining the inner edge a 1 μm wide marker is placed into the section plot as a starting point and centered the x-y curves with this marker, as indicated in figure 2.4. As one can

see in figure 2.4 the outer halo rises from a few tenth of a nanometer up to a height of approximately 1.8 - 2 nm. This is approximately the size of a typical Pt nanocrystal deposited via EBID (see chapter 1.1, hence, assumed to represent a deposit monolayer. Due to the averaging of the sections of the structures over 500 nm along Y, lower heights than the one monolayer height were observed, due to a laterally nonclosed film.

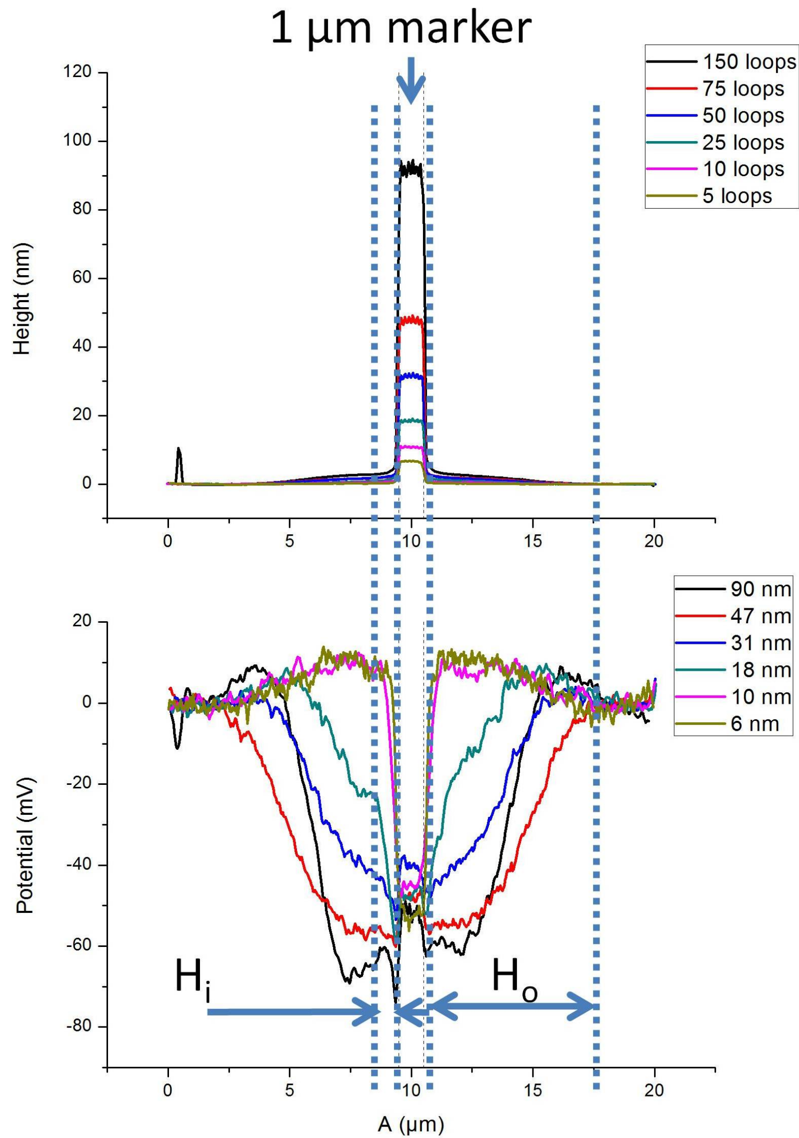

Figure 2.4: Topography and KPFM line section over the deposits with 30 keV showing the 1 μm wide marker for defining the inner edge.

The results for H_{edge}, H_i and H_o radius in dependency on the deposit height are shown in figures 2.5 to 2.7. On the left side in figure 2.5 one can see the according Monte Carlo

simulation [15] of the BSE radius for comparison and consolidating our concept. As one can see, the outer halo is steadily increasing with an asymptotic character. This asymptotic outer halo radius matches the simulated radius of BSE in good agreement. This saturating behaviour can be explained by the low number of electrons impinging, and contributing to BSE yield, for thin structures, resulting in an outer halo radius much smaller than the simulated BSE radius. As the structure's height increases, the total number of (BSE) electrons increases as well and the outer halo approaches to the simulated value.

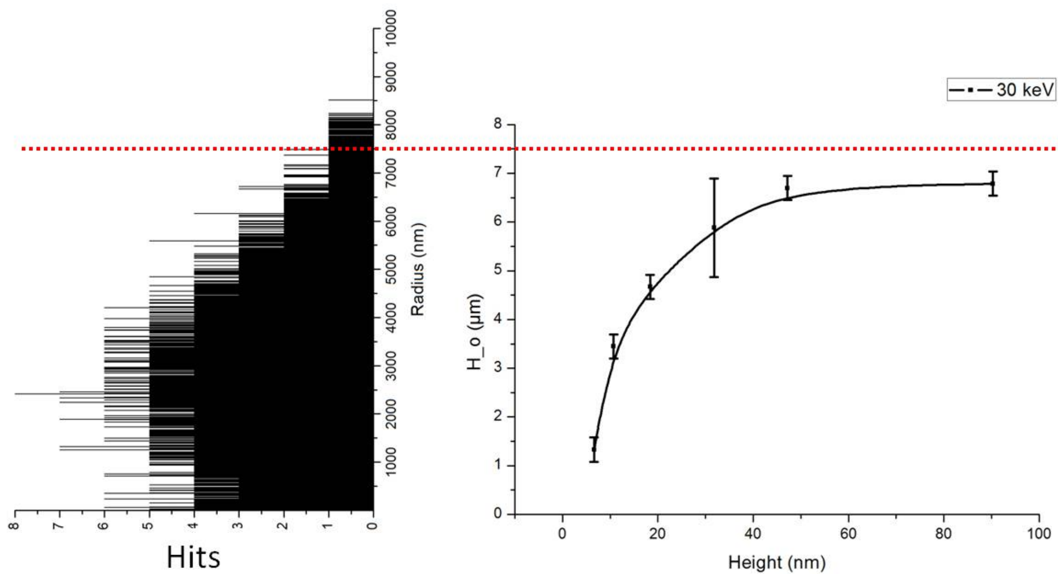

Figure 2.5: Experimentally determined outer halo radius for the 30 keV structures (right) with simulated radius of backscattered electrons (left).

H_{edge} describes the intrinsic deviation of the structure's side wall slope, mainly due to secondary electrons (**SE**). As one can see in figure 2.6, already for sub-10 nm structures, there is an intrinsic limitation of the structure's slope broadening. For structures deposited with 30 keV this limit is approximately 75 nm for the thinest deposit. For higher structures this intrinsic limitation grows up to 150 nm for a deposit height of 90 nm. The measured values are always larger than 75 nm, though the SE range is 25 nm. Hence, another effect is responsible for this additional broadening: the SE are generated not only by the primary electrons (**PE**), but also by scattered electrons within the structure. These electrons also generate SE in the already broadened deposit slope, resulting in an

increased edge halo, broader than the actual SE range relativ to the intrinsic deposit edge.

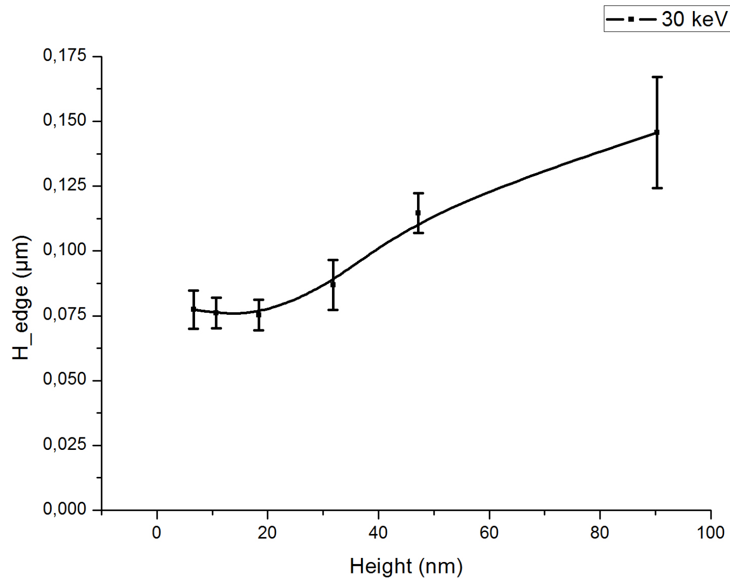

Figure 2.6: Experimentally determined edge halo H_{edge} radius for 30 keV deposit.

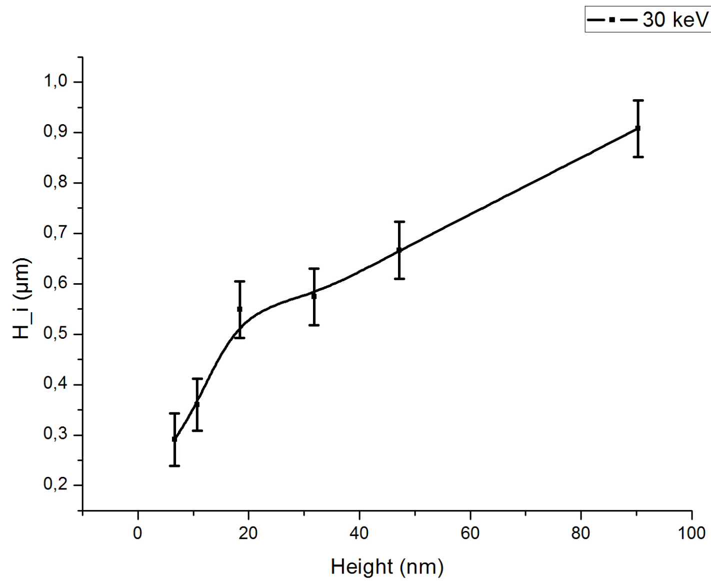

Figure 2.7: Experimentally determined inner halo H_i radius for 30 keV deposit.

H_i is formed by FSE and is not strongly developed at 30 keV, because at this acceleration voltage, the electrons penetrate through the already deposited structure without

many interactions, resulting in only a few FSE for additional deposition. As one can see in figure 2.7, H_i increases nearly linear from approximately 275 nm, for the sub 10 nm deposit, to approximately 900 nm, for the 90 nm structures. This increasing behaviour can also be explained by the total number of electrons contributing to forward scattering, increasing linear with the deposit height.

For ensuring not to run into the limitation of the AFM tip opening angle (see chapter 1.2), figure 2.8 shows a drawing of the Si probe with an tip opening angle of $\approx 30°$ at the edge of a 100 nm pad, neglecting the tip radius of 5 nm. At 100 nm deposits, for which the angle of the slope gets closest to the limitation, the tip angle related limitation at the bottom is ¡ 30 nm, which is far away from the smallest measured value of the innermost halo, confirming that even the most critical values, measured via AFM, are not entirely driven by the AFM tip (although an influence is definitely present).

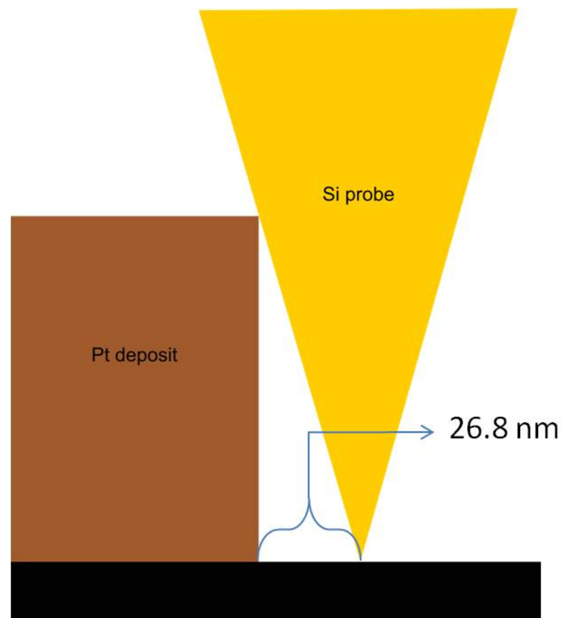

Figure 2.8: Schematic drawing of the geometric tip limitation for a structure with a height of 100 nm.

Further investigations using Kelvin Probe Force Microscopy (**KPFM**) serve as tool for distinguishing different chemical composition of deposited material. In figure 2.9 a KPFM image (bottom left) and a corresponding line section of the structure with the halo can be seen (bottom right), together with the corresponding height image and cross section (top left and right, respective). In the center a 1 μm marker is shown for relating the intended dimension of the deposit to the proximity effects. As one can clearly see the

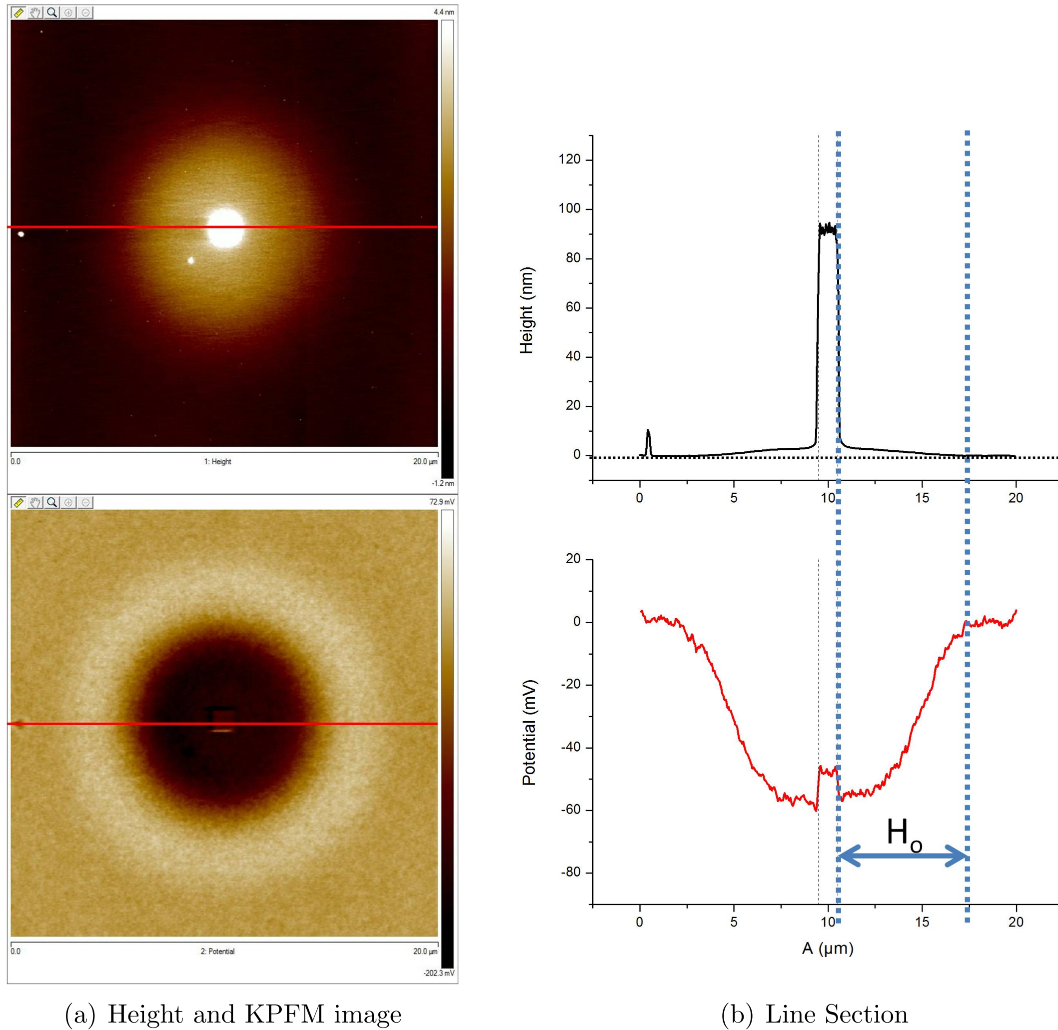

(a) Height and KPFM image

(b) Line Section

Figure 2.9: KPFM (a) and line section (b) image of investigated structure showing the forming of two plateaus, one at the pad itself and one at the halo.

pad itself forms a plateau in the surface potential scan. In contrast, the outer halo forms a plateau at a different value compared to the actual pad, suggesting strongly that the chemistry is different from the actual deposit and thus having a different surface potential. We can exclude that the H_o plateau is a substrate related effect, due to the fact, that it is below the level of the Pt deposit. If it was a substrate related effect, the halo plateau should be between the substrate level and the pad level. Hence, we can conclude, that the halo consists of a different chemistry, most likely composed by incomplete dissociated precursor molecules. The measured potential of the halo and the structure is slightly different from the effective potential, due to long range cantilever contribution (see section 1.2.3), thus approaching the two plateaus to each other.

In figure 2.10 (a) one can see the line cross sections of the 20 keV structures, whereas in (b) the center of the line cross section is zoomed-in for revealing the inner halo and its surface potential. As one can see, beside some edge effect, which appears in the decreasing behaviour shortly outside the pad, the inner halo forms a level, which is very similar to the plateau formed by the pad itself. Due to having nearly the same level, we can conclude that the inner halo is of a similar chemical composition compared the pad to Pt. The slight decrease can be explained by the influence of the outer halo level to the inner halo level, which may be a result of the long range cantilever contribution.

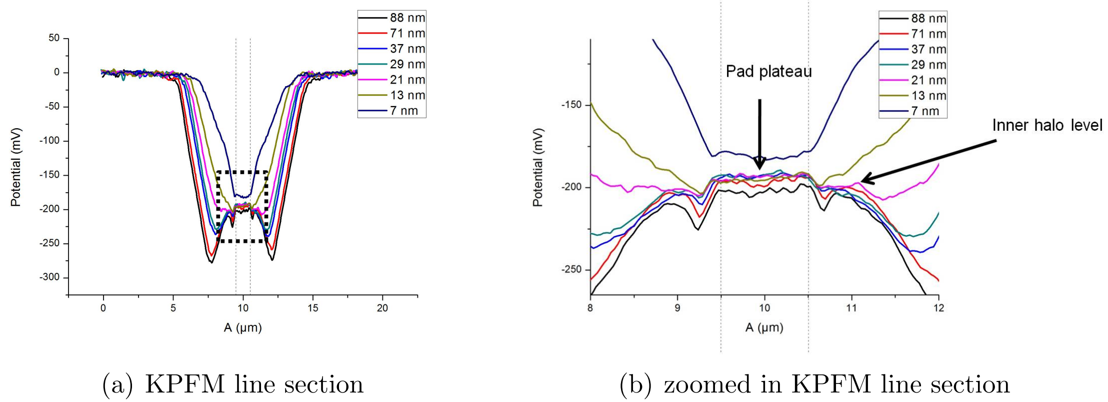

(a) KPFM line section

(b) zoomed in KPFM line section

Figure 2.10: KPFM line cross section of 20 keV deposits (a) and closer look to the center of the line cross section (b) for revealing the inner halo level.

2.2 Electron energy and height variation

To allow for an comprehensive insight about the intrinsic limitations for the lateral resolution the electron energy of the deposition was variied from 5 keV up to 30 keV in 5 keV steps. This variation in acceleration voltage affects the average penetration depth of electrons in the solid (Bethe range) resulting in a different interaction volume of the electrons in the relevant materials. As a consequence, the outer halo will change it's size due to the surface radius of BSE, and the inner halo will get affected due to the changed forward scattering probability at the deposit height.

For getting an idea about the development for the different halos and for deriving sophisticated design rules for the different electron energies, we varied the depositions heights from sub-10 nm up to approximately 100 nm. First of all, as demonstrated in chapter 2.1, the height dependency on the loop number was determined. These functions are summarized in table 2.1 to provide comparable pad heights for all electron energies.

acceleration voltage [keV]	**function** [#]	**point pitch** [nm]	**dwell time** [μs]	**beam current** [pA]
5	$h = 0.39 \cdot l$	14.9	100	98
10	$h = 0.29 \cdot l$	11.58	100	130
15	$h = 0.33 \cdot l$	9.69	100	140
20	$h = 0.36 \cdot l$	8.6	100	150
25	$h = 0.29 \cdot l$	7.75	100	150
30	$h = 0.61 \cdot l$	7	100	150

Table 2.1: Summary of height vs. loop number functions, derived from AFM measurements. (h... height (nm), l...loop number)

Comparing the height sections of the particular structures in figure 2.11 to each other, one can see, that the halo's shape is changing. At 30 keV just a low, nearly flat halo can be seen, with a sharp edge at the bottom of the structure. As the electron energy is decreased one can observe an increasing halo height forming some additional edge at 20 keV and 15 keV, resulting in a second slope without an additional edge at even lower electron energies. This reflects the transition from BSE to FSE dominated broadening, as we show later in detail. At 5 keV only a broadening of the structures bottom can be observed, which is predominantly caused by FSE. So the predominant electron species for the proximity deposition for sub 100 nm deposits changes from BSE to FSE for decreasing primary electron energies.

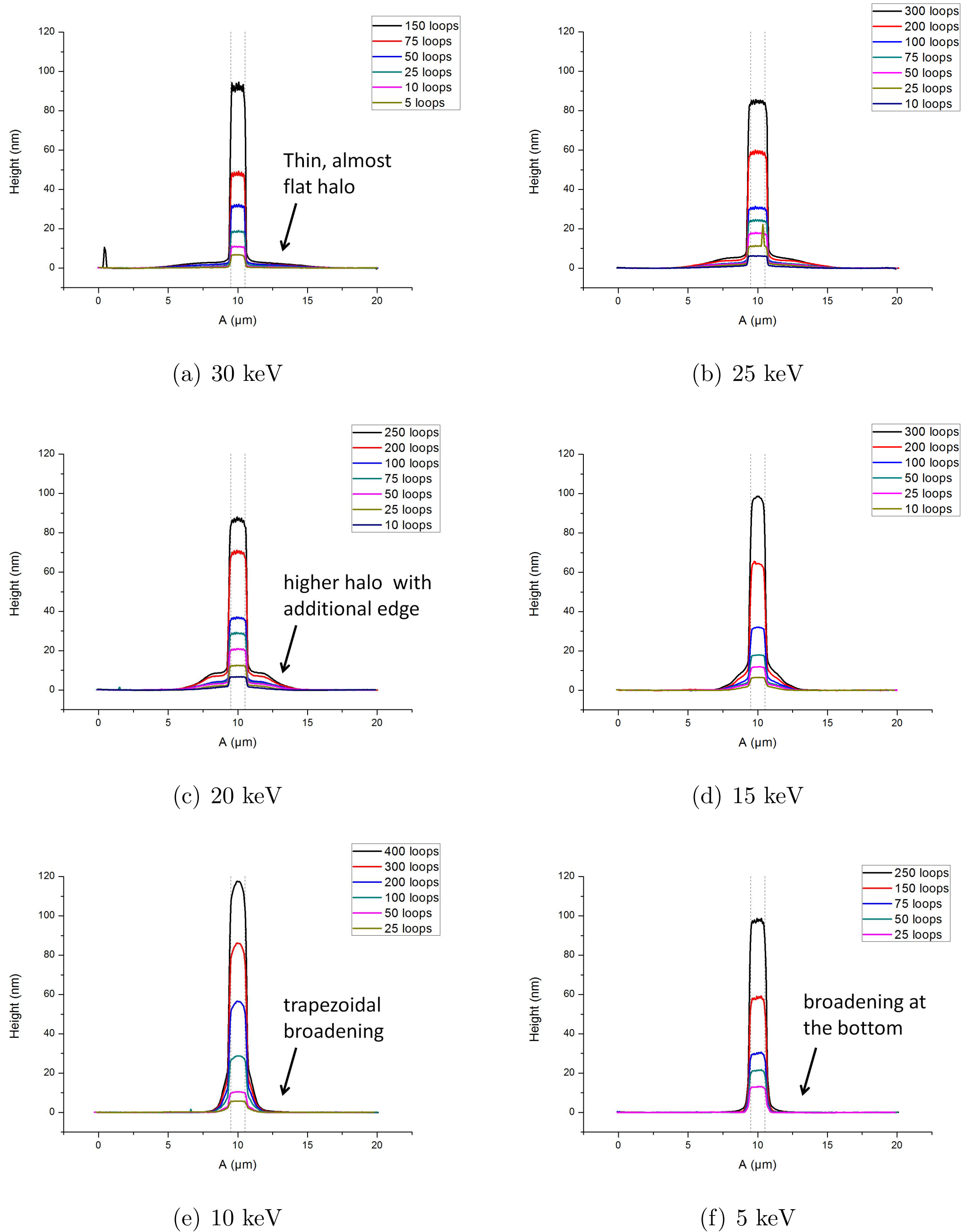

Figure 2.11: Comparison of height sections at different electron energies for varying deposit heights.

2.2.1 Outer halo development

Since the formation of the outer halo is driven by backscattered electrons and their radius is changing with the acceleration voltage, a variation of the outer halo radius can be expected for decreasing electron energies. As one can see in table 2.2, the simulated radius of the backscattered electrons[1] grows from 0.4 μm at 5 keV up to 7.5 μm at 30 keV for Si substrates with a 3 nm SiO_2 layer on top.

acceleration voltage E_0 [keV]	r_{BSE} [μm]
5	0.4
10	1.2
15	2.4
20	3.9
25	5.8
30	7.5

Table 2.2: Simulated development of the outer halo at the used acceleration voltages on the Si substrate.

This variation is expected to be seen at the outer halo measurements. As discussed in section 2.1 and shown in figure 2.12 by the olive graph the outer halo for 30 keV structures grows asymptotically towards a value of approximately 7 μm, which is similar to the simulated value of 7.5 μm in table 2.2 for increasing deposit heights. One would expect the same attitude for the other structures outer halo.

As one can see in figure 2.12 (b) the behaviour of the 30 keV structures can not be observed for all energies. At higher energies ranging from 30 to 20 keV, H_o grows steep with an asymptotiv behaviour as the deposit height increases. For such high electron energies, the deposition of sub 100 nm structures is predominated by BSE. However, for energies lower than 15 keV another increase after the first asymptotic behaviour can be observed. At 5 keV there is a plateau for the thinnest deposits, which runs over to a nearly linear growth for higher deposits. For lower electron energies ranging from 15 to 5 keV the predominated electron species changes from BSE to FSE. At 15 keV the crossover can be seen very cleary (see figure 2.12). This FSE caused halo building will be discussed in the following section.

In figure 2.12 (c) the outer halo radius is plotted in dependency on primary electron energies for different heights together with Monte Carlo simulations (green spheres). For

[1] simulated with CASINO [31]

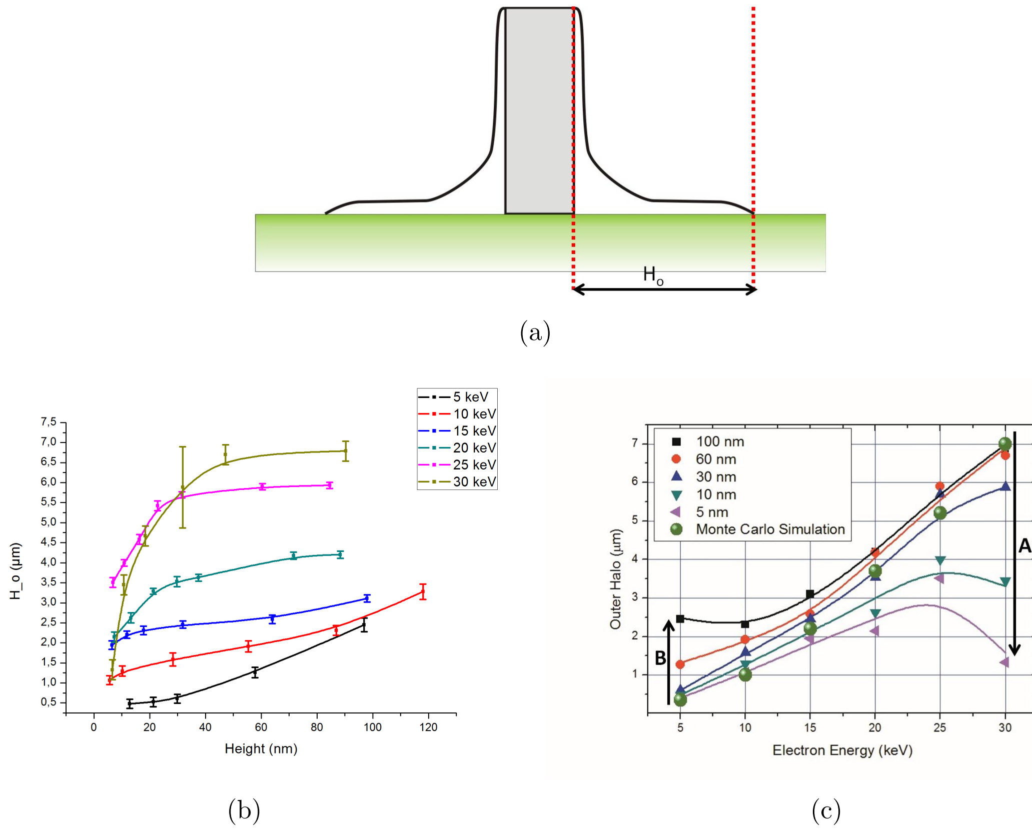

Figure 2.12: (a) Schematic illustration of the outer halo. (b) Comparison of the outer halo radius for the used acceleration voltages. (c) Maximum diameter of proximity deposition for different electron energies and deposit heights together with Monte Carlo reference simulations, revealing an efficiency related downturn for high energies / thin deposits (A) as well as a forward scattered electron related upturn for low energy / high deposits (B).

thin deposits one can clearly see that the outer halo decreases at high electron energy, as indicated by the arrow A. This downturn is related to the decreasing deposition efficiency for high electron energies, due to small effective cross sections for a deposition event. In contrast, thick deposits show an upturn of the outer halo for low energies, as indicated by the arrow B, due to the FSE related outcoupling skirt. At low PE energies the electrons escape the structure more likely, thus forming this upturn. This occurs, because of the electrons getting scattered much more easily for low energies, resulting in a high number of forward scattered electrons for these heights.

2.2.2 Edge halo and inner halo development

In figure 2.13 the results of the measurements of the edge halo are shown for all electron energies. By plotting the data in dependency on the height, as shown in figure 2.13 (b), one can clearly see that no clear trend for the development of the edge halo could be found in this plot, due to the mixed up edge halo radius for the different electron energies. Alternatively, we plotted the data in dependency on the PE energies for different heights, as we did for the outer halo, which can be seen in figure 2.13 (c). Out of this plot one can determine similar systematic behaviour for all heights. As one can clearly see, there is no monotonic behaviour, with a minimal value at 30 keV for all heights, which rise the question for the origin of this unexpected behaviour.

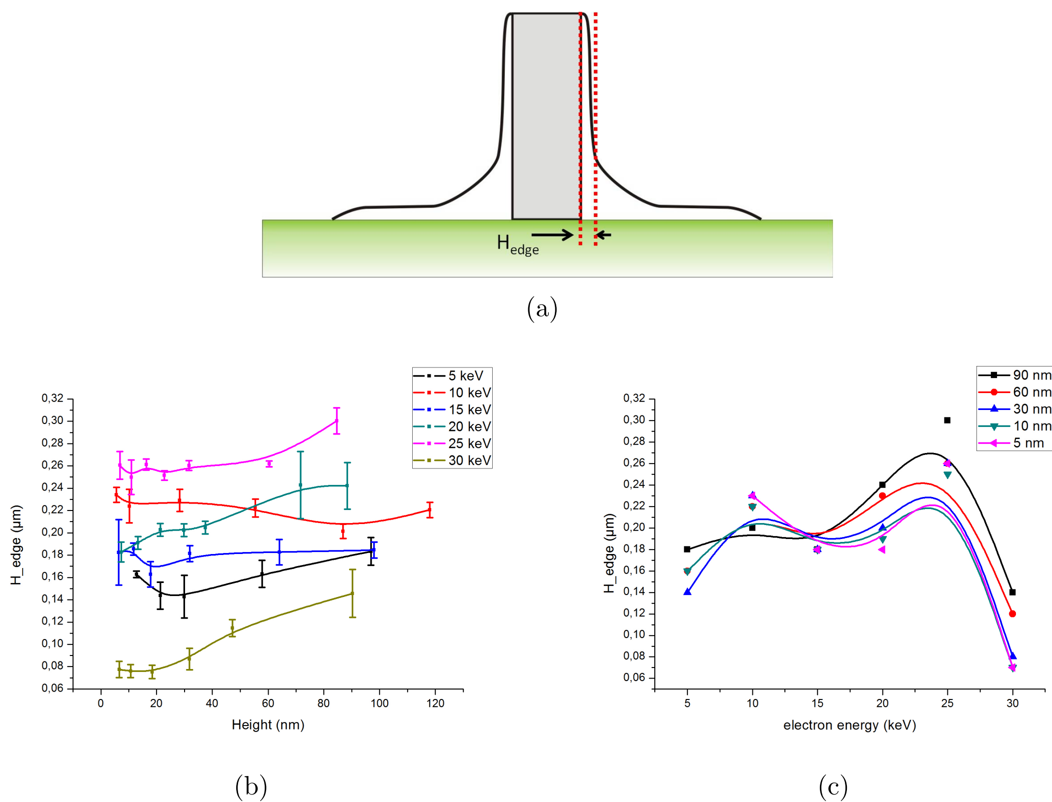

Figure 2.13: (a) Schematic illustration of the edge halo. (b) Comparison of the edge halo radius for the used acceleration voltages. (c) Measured H_{edge} data plotted in dependency on the electron energy for different heights.

As the shape of the halo is varying severly and forming no definite edge, the measurements of the inner halo H_i turned out to be difficult. As the inner halo grows with other properties than the outer halo exceeding it for small electron energies, the radius of the

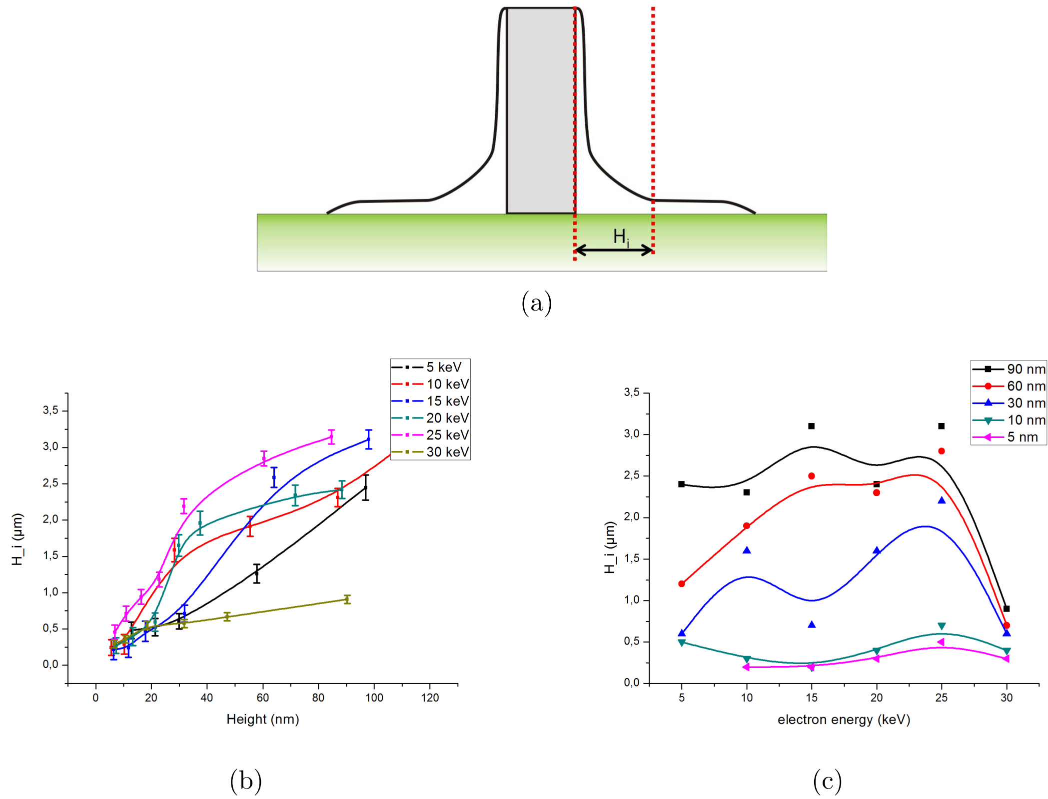

Figure 2.14: (a) Schematic illustration of the inner halo. (b) Comparison of the inner halo radius for the used acceleration voltages. (c) Measured H_i data plotted in dependency on the electron energy for different heights.

inner halo is set the same as the outer halo in such cases. In figure 2.14 one can see the data of the inner halo measurement. In figure 2.14 (b) the measured data is plotted in dependency on the height. As for the inner halo, out of this plot no systematic behaviour can be determined beside of the continuously increasing trend. Hence, the data have been plotted in dependency on the PE energy, as shown in figure 2.14 (c), revealing a similar trend as for the edge halo, however, with a strong height dependency. Again, the smallest value of the radius was observed at the 30 keV deposits, but this time for smaller electron energies, the radius is much more sensitive on the deposit height for smaller energies. As one can see, for 15 keV the radius stays relative small for deposit heights up to 30 nm, but increases steeply for higher deposits.

Since the inner halo is assumend to be formed by FSE's and the shape of the halo is quite different for the used electron energies, further considerations focus on the amount of patterning points which contribute to the deposition with FSE character independency on the electron energy, as shown in figure 2.15. So the main question is, from which

spatial point (x,y,z) the electrons can contribute to FSE events at point X. For estimating this number of points, a simulation of electrons, impinging a 100 nm Ti-layer was made. Note, that Ti shows a resulting Z identical to a typical Pt/C atomic ratio of 15/85. Out of these simulations, shown in figure 2.16, one can estimate the radius of the main FSE contribution, which can escape the structure at the side walls and cause some additional deposition, which is summarized in table 2.3.

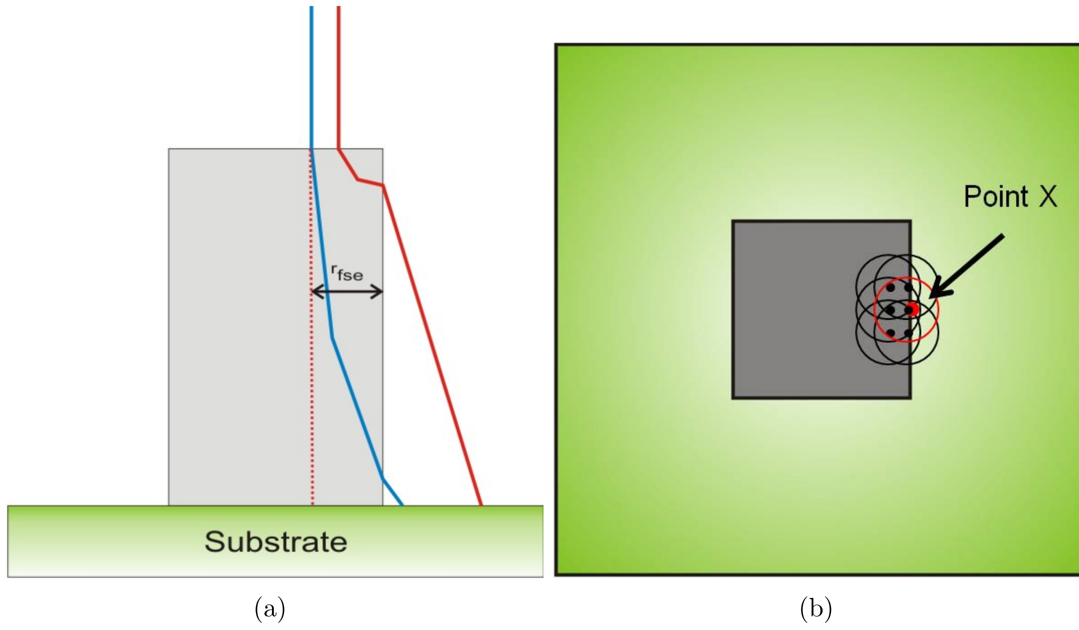

(a) (b)

Figure 2.15: (a) Schematic ilustration showing the contribution to forward scattering for high(blue) and low(red) electron energies. (b) Schematic topview drawing of electron impinging points contributing to forward scattering at point X.

acceleration voltage [keV]	$\mathbf{r}_{fse}$ [nm]	**number of points** [#]
5	≈ 200	≈ 280
10	≈ 400	≈ 1870
15	≈ 400	≈ 2680
20	≈ 300	≈ 1910
25	≈ 300	≈ 2350
30	≈ 200	≈ 1280

Table 2.3: Simulated radius of electrons contributing to forward scattered additional deposition.

With this estimation of the lateral contribution radius r one can calculate the number of points, which provide the main contribution to building of the inner halo at point X

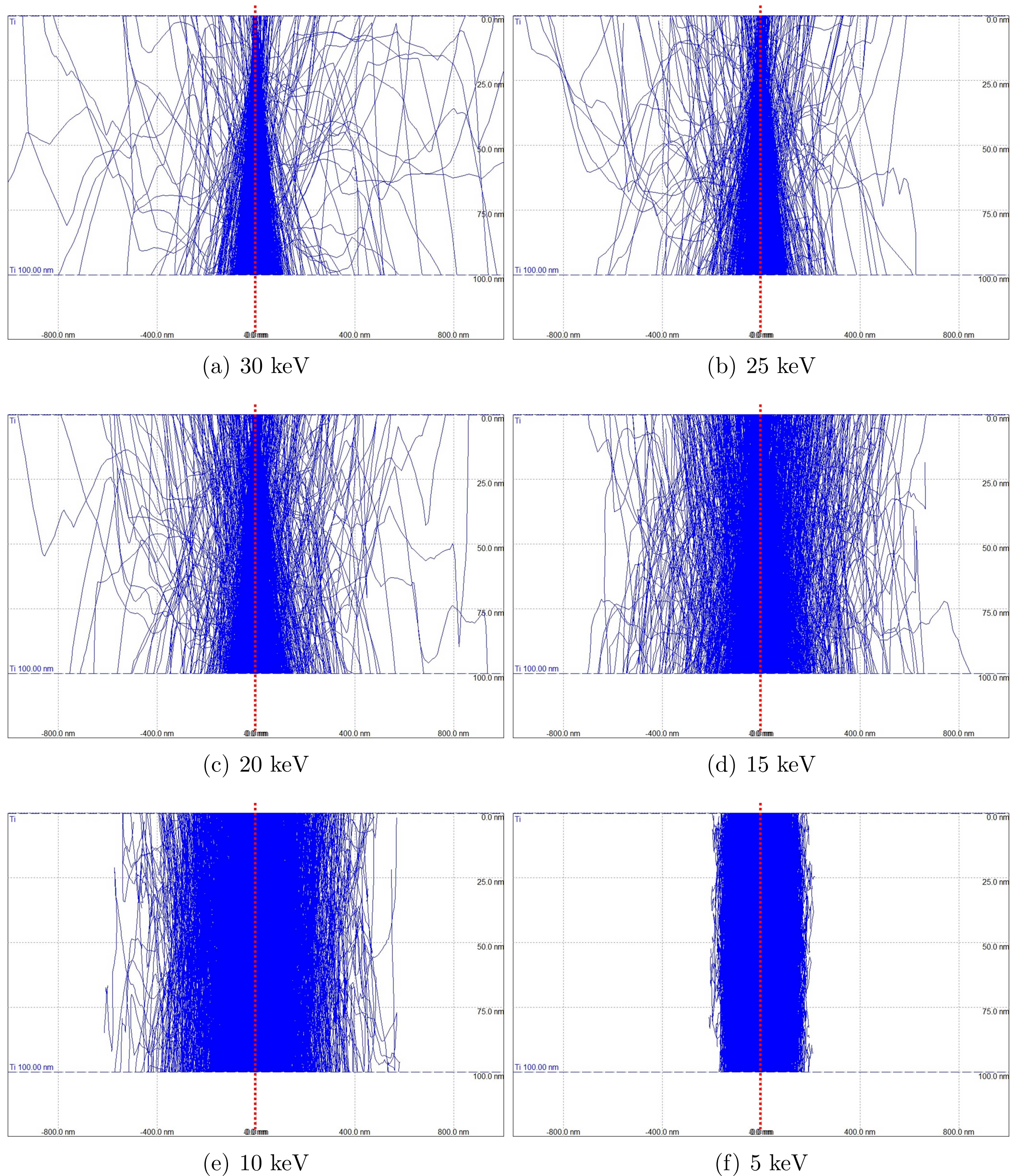

(a) 30 keV

(b) 25 keV

(c) 20 keV

(d) 15 keV

(e) 10 keV

(f) 5 keV

Figure 2.16: Simulation of electron trajectories in 100 nm Ti for estimating the number of points contributing to forward scattering effects. The data is plotted with the indentical scale for the different electron energies.

using the applied point pitch, according to table 1.5. The last column of table 2.3 gives the number of patterning points which can eventually contribute to deposition events at

the point X. This number is calculated out of half the area of a circle, shown in figure 2.15 (b), with the radius shown in table 2.3 divided by the square of the point pitch for each energy. With the known number of points and the known number of electrons for each point, derived from the given beam current and the dwell time, the number of electrons per loop that may contribute to the additional deposition can be estimated, as listed in the last column of table 2.4. This number of represents an estimation of forward scattered electrons for each point X (at the deposit edge) which can contribute to the deposition. At the corner it will be lower, due to a reduced number of adjacent points, which can explain that the FSE related inner halo is not of perfectly rectangular shape.

acceleration voltage [keV]	**electrons per point** # [$\cdot 10^4$]	**electrons forward scattered per loop** # [$\cdot 10^6$]
5	$\approx$ 6.11	$\approx$ 17
10	$\approx$ 8.11	$\approx$ 152
15	$\approx$ 8.73	$\approx$ 234
20	$\approx$ 9.36	$\approx$ 179
25	$\approx$ 9.36	$\approx$ 220
30	$\approx$ 9.36	$\approx$ 120

Table 2.4: Simulated radius of electrons contributing to forward scattered additional deposition.

Figure 2.17 shows the estimated number of electrons that may contribute to forward scattering at one point X at the structure edge. As one can see, the 5 keV and 30 keV value is very much smaller than for the other electron energies. First of all, at 5 keV the given beam current is the lowest and the point pitch is the highest compared to the other electron energies, resulting in the least number of electrons impinging at one point and the lowest number of patterning points contributing, which results in this minimal number of electrons that may contribute to forward scattering. On the other hand, at 30 keV the point pitch is the smallest and the beam current is highest of all energies, but the low number of electrons that may escape the structure results from the probability of getting scattered in the 100 nm layer. For high PE energies, the electrons penetrate through the already deposited structure without many interactions, resulting in a low forward scattered contribution radius and thus in few forward scattered electrons.

Out of this estimation one can see, that for the 5 keV structures the effect of forward scattered electrons is smaller compared to the structures from 15 up to 25 keV as a result

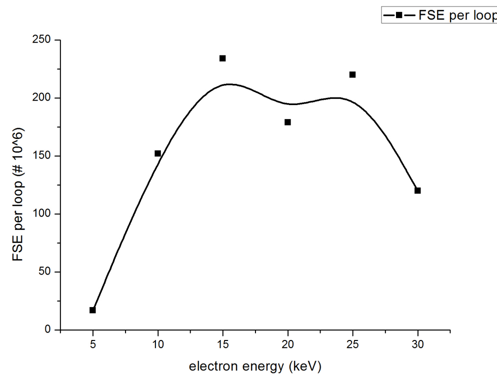

Figure 2.17: Electrons contributing to forward scattering per loop for one point at the edge of the deposit with 100 nm height and thus contributing to the building of the edge and inner halo for different electron energies and used deposition parameters.

of fewer electrons contributing to the additional deposition. This is in consistence with the height images shown in figure 2.11 and the measurements of the edge and inner halo, shown in figure 2.13 and 2.14. Also for the 10 and 30 keV structures the magnitude of the effect is in between the extremum.

2.2.3 KPFM comparison

As discussed in chapter 2.2.1, the outer halo scales with the energy of the electrons impinging. This fact is verified by the KPFM plots shown in figure 2.18. Due to the sensitive parameter of tip - sample distance, generally only potential differences instead of absolute values are reliably accessible.

As one can see in figure 2.18, a plateau is formed by the pad itself for every electron energy. Due to some variance in the composition of the pad, this plateau isn't at the same absolute value for the different energies, so one can only compare the different energies qualitatively. However, what can be reliably distinguished is a second plateau formed by the outer halo, which lies under the plateau formed by the pad. This could not be observed for the 5 keV deposits, due to the small diameter of the outer halo which is screened by the inner halo. With increasing the electron energy the outer plateau is getting wider, resulting in a well distinguishable plateau at 30 keV.

The inner halo has a potential, which is quite the same as the potential of the pad and can bee seen clearly in the structures from 15 - 25 keV, showing values similar compared

to the actual pad, as shown in figure 2.10 for the 20 keV deposits in detail. This value of the inner halo can be seen just outside of the edge of the pad beside some edge effect.

So one can estimate that the material deposited by the forward scattered electrons is quite the same as the pad itself, whereas the material forming the outer halo has a different surface potential. This leads to the conclusion, that a considerable fraction of this part contains incompletely dissociated precursor fragments, due to the low number of BSE, resulting not likely in two or more dissociation events on the same point.

Since a different chemical conposition should result in different functional properties, we made further investigations using the conductive AFM module for resolving the conductivity laterally and making statements about the conductivity of the different halo types for the Pt deposits. This investigations is subject of the following section 2.2.4.

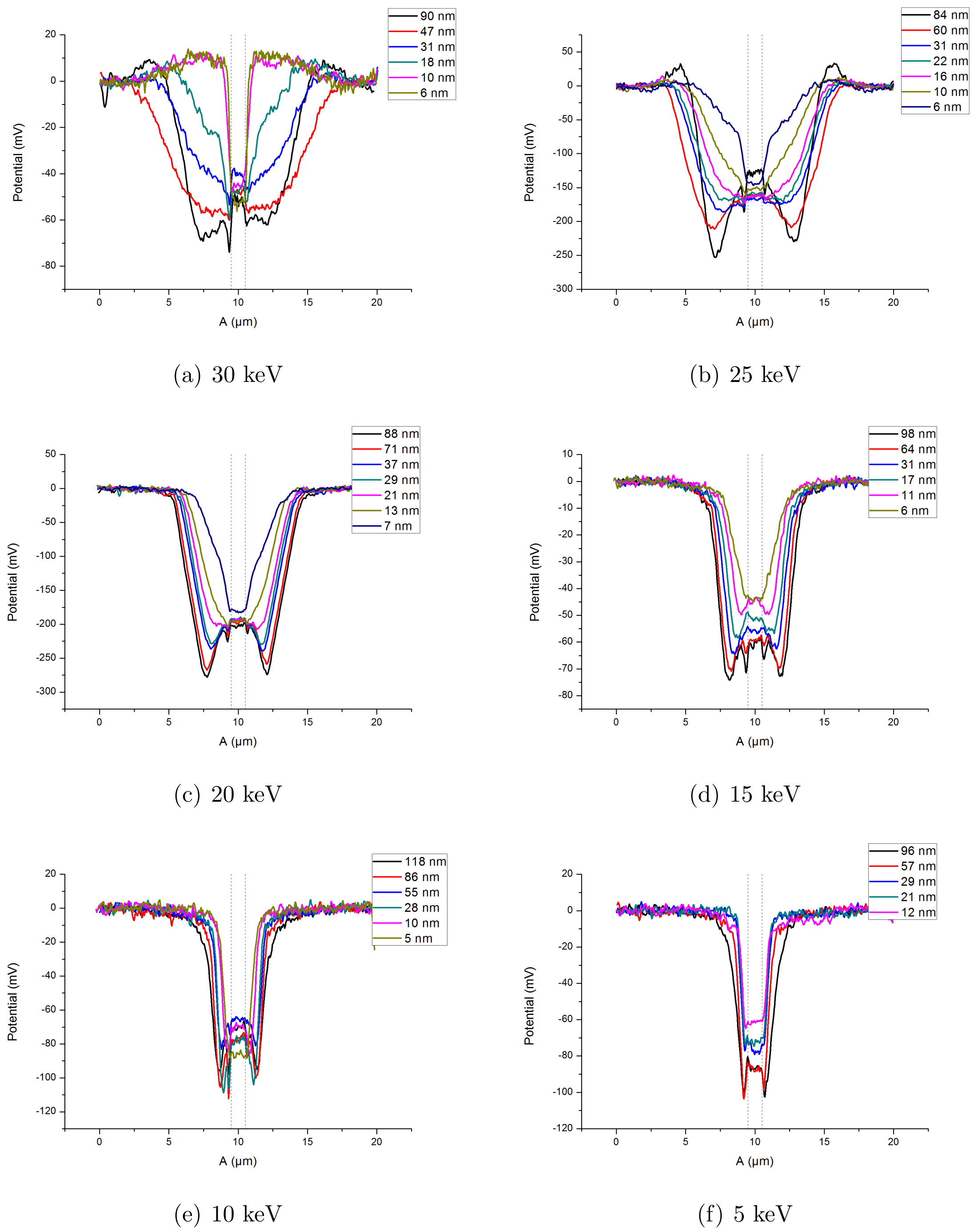

(a) 30 keV

(b) 25 keV

(c) 20 keV

(d) 15 keV

(e) 10 keV

(f) 5 keV

Figure 2.18: Comparison of KPFM sections at different electron energies for varying deposit heights.

2.2.4 Conductive AFM measurements

Further investigations concerning the conductivity of the deposits and its unwanted halos were done with C-AFM. This tool allows for imaging the conductivity laterally resolved measurements simultaneously with the morphology, so one can visualize the resolution limitations for deposits due to electrically conductive halos. As shown in figure 1.36 the structures were deposit across a conductive Au - path.

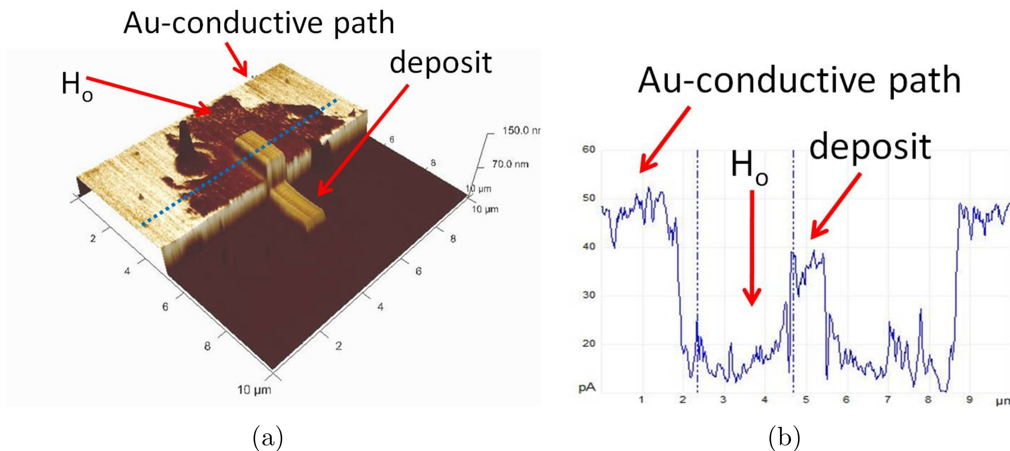

(a) (b)

Figure 2.19: C-AFM Measurement of a Pt deposit with 30 keV, revealing the variance in conductivity between the Pt - deposit,the Au - conductive path and the non-conductive halo. (a) 3D Image of the topography with the conductivity as color overlay. The bright parts reveal the high conductive areas, whereas the dark areas are less conductive. (b) Line Cross section of the current along the indication in (a).

In figure 2.19 one can see a 3D image of a Pt deposit measured with C-AFM. The color indicates the current (conductivity) with the bright areas as higher conductive parts. The non-conductive outer halo can be seen very clearly, which is, however, not totally zero, due to some tunneling through currents the very thin outer halo (¡2 nm) and the underlying gold path. The radius of the outer halo is similar to the radius measured on the Si-substrate, because the Au - conductive path has only a height of approximately 50 nm, which will not affect the radius of backscattered electrons severly.

As can be seen by the cross section in 2.19, the conductivity of the Pt deposit is lower than the conductivity of the Au - path. This is a result of not having pure Pt within the the deposit, but Pt nano crystals embedded in a carbon matrix as discussed in chapter 1.3, revealing a non-metallic behaviour.

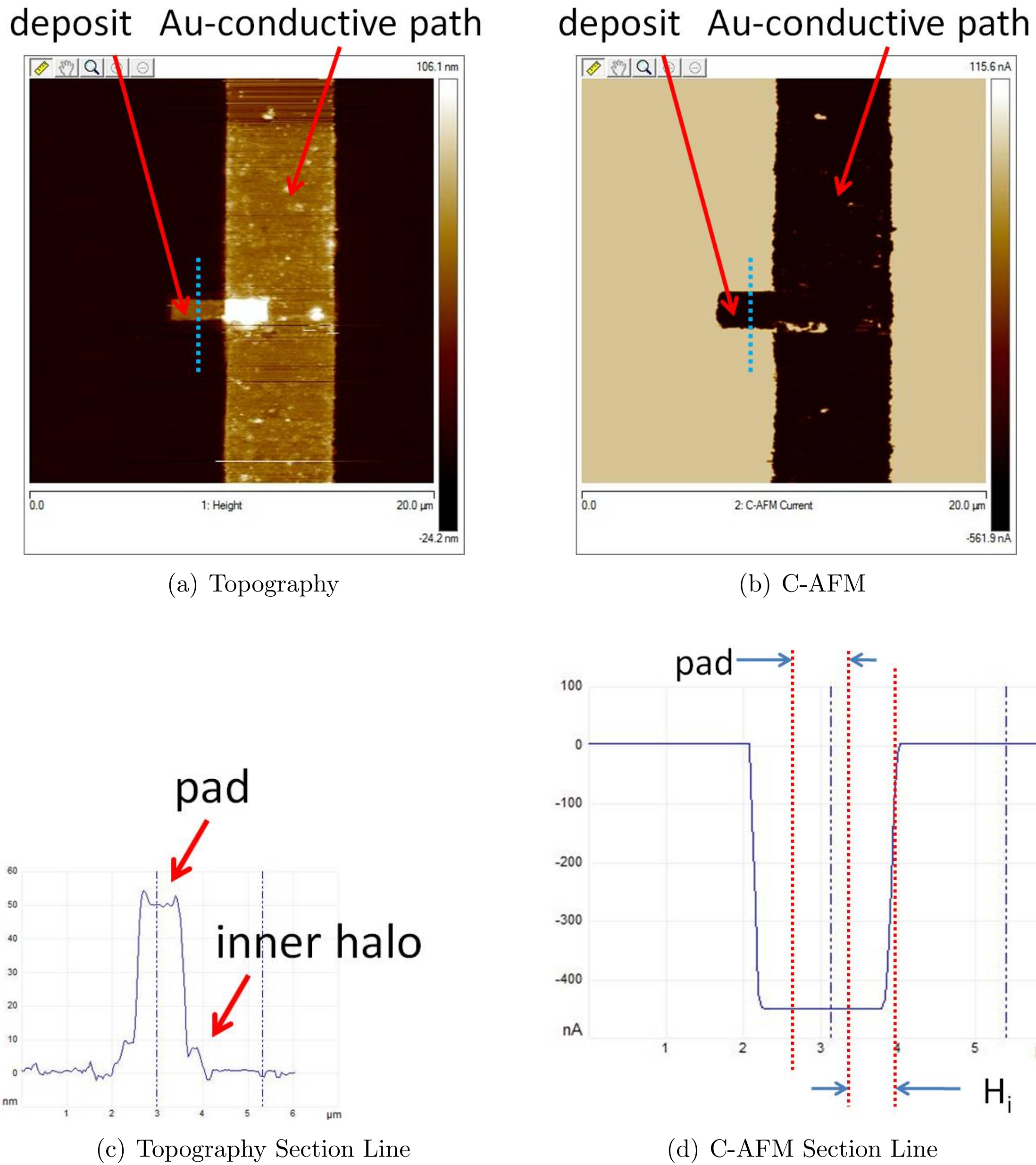

(a) Topography

(b) C-AFM

(c) Topography Section Line

(d) C-AFM Section Line

Figure 2.20: Height (a) and C-AFM measurement (b) of a Pt deposit at 5 keV. In (c) and (d) line cross sections from the indicated areas in (a) and (b) are plotted for revealing the inner halo conductivity.

To access the inner halo and its conductivity, a 5 keV deposit have been prepared. The conductivity measurement in figure 2.20 were done by applying the maximum voltage of - 12 V for getting an clear edge between the conductive and non-conductive deposit. Due to the negative voltage, the conductive part of the structure will appear as dark area,

because the current is negative. The width of the structure at the topography image with $\approx 1\ \mu$m, as initially designed, has to be compared with the width of the conductivity image, which is $\approx 1.9\ \mu$m as indicated in figure 2.20. This is nearly twice the designed deposit width, which allows for the conclusion that the inner halo, caused by FSE, is highly conductive and hence the limiting factor for maximum lateral resolution which is discussed in chapter 3 in details. So one has to look at the inner halo radius limitating conductive path designing, which is discussed in detail in the following section.

3 Discussion

As experiments reveal, the additional but unwanted deposition has to be subdivided into three different types, according to their shape. Figure 3.1 shows a schematic drawing of the three different types of the unwanted deposition. First of all there is the edge halo H_{edge}, which is a broadening of the vertical side wall into a trapezoidal cross section. The second deviation is the outer halo H_o, which is a wide but flat additional deposition. The third type is in between the edge and outer halo, and is called the inner halo H_i, which is an additional deposition on the bottom of the structure varying the bottom edge of the deposit on top of the outer halo.

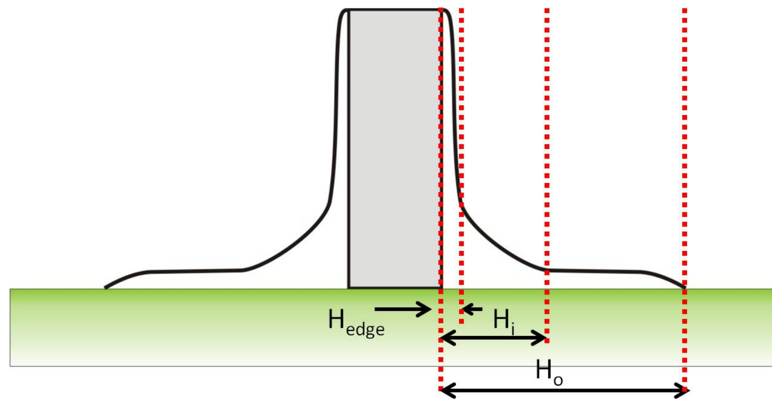

Figure 3.1: Schematic classification of deposited structures showing the inner, outer and the edge halo.

To explain the formation of these three halos, the electron scattering events and thus the different electron species with their different implications for proximity depositions have to be considered. First of all, there are the primary electrons (**PE**), which cause the first deposition events (see figure 3.2). However, the cross section of the high energy PE for precursor dissociation is very small [29], hence, very unlikely. These PE generate secondary electrons SE_I at a scattering event within the solid, which can contribute to deposition at the surface side wall, when generated in a depth of less than 25 nm with respect to the surface (SE range). The cross section of low energy SE is ideal for

precursor dissociation, so this type of deposition will be very efficient. As the PE beam is further scattered, it can happen that it can escape the deposit again, resulting in forward scattered electrons (**FSE**), where also additional deposition is possible. These FSE impinge onto the surface and can cause another deposition event, however, with a low probability. Due to the high energy of the PE, they can alternatively penetrate through the actual deposit into the substrate, where they can get backscattered, resulting in additional deposition events backscattering electrons (**BSE**$_{II}$) and related SE$_{II}$ contributions. Additional BSE can also occur within the deposit leading to BSE$_{I}$ and according SE$_{II}$ generation, as shown in figure 3.2.

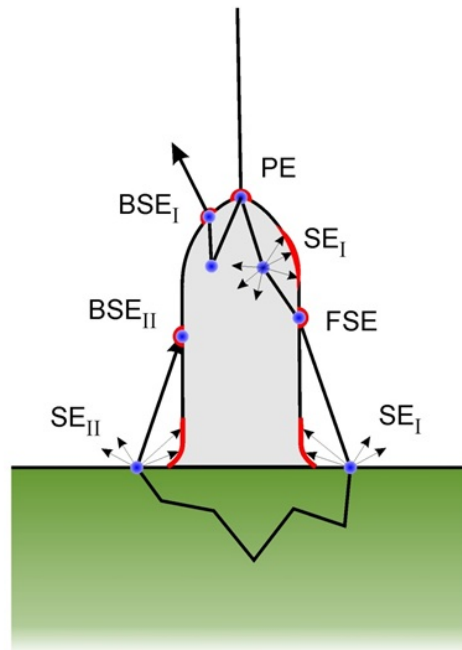

Figure 3.2: Schematic drawing of deposition events due to different electrons [14]

For characterisation of the different halos we varied the electron energy from 5 - 30 keV and the height of the deposit from sub-10 nm up to approximately 100 nm. In figure 2.11 the topography line cross section of the different electron energies are summarized.

At 30 keV just a thin, almost flat halo can be seen, with a sharp edges at the corner to the deposit. As one can see in the oliv graph of figure 3.3, the outer halo starts with a sharp increase for thin deposits and ends in an asymptotic behaviour for high structures. This asymptotic value of approximately 7 μm is in good agreement to the simulated radius of BSE with 7.5 μm. The sharp increase for thin deposits is a result

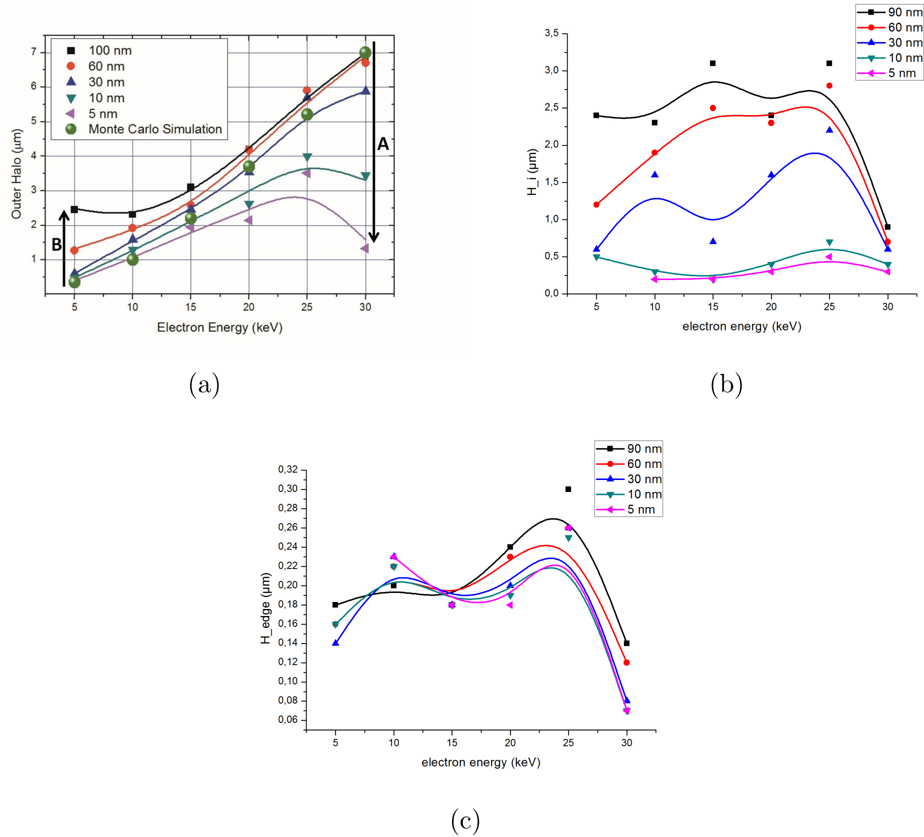

(a)

(b)

(c)

Figure 3.3: (a) Maximum diameter of proximity deposition for the outer halo for different electron energies and deposit heights together with Monte Carlo reference simulations, revealing an efficiency related downturn for high energies / thin deposits (A) as well as a forward scattered electron related upturn for low energy / high deposits (B). (b) Inner halo measurement for different electron energies and deposit heights (c) Edge halo measurement for different electron energies and deposit heights

of low number of PE which entail an even lower number of BSE, resulting in an outer halo radius much smaller than the simulated radius. As one can see in figure 3.3 (b), the inner halo ranges from ≈ 250 - 950 nm with a strong height dependency, while the edge halo (figure 3.3) ranges from ≈ 75 - 150 nm with an energy dependency. An important observation is the behaviour for 30 keV, which shows lowest values for H_{edge} (figure 3.3 (c)) and weakest height dependencies for H_i (figure 3.3 (b)). The former is caused by SE, generated by PE and FSE, while the later is a result of FSE.

The 15 keV deposits show a very special behaviour for the line cross sections based on the developement of the different halo types. At the topography images in figure 2.11 one

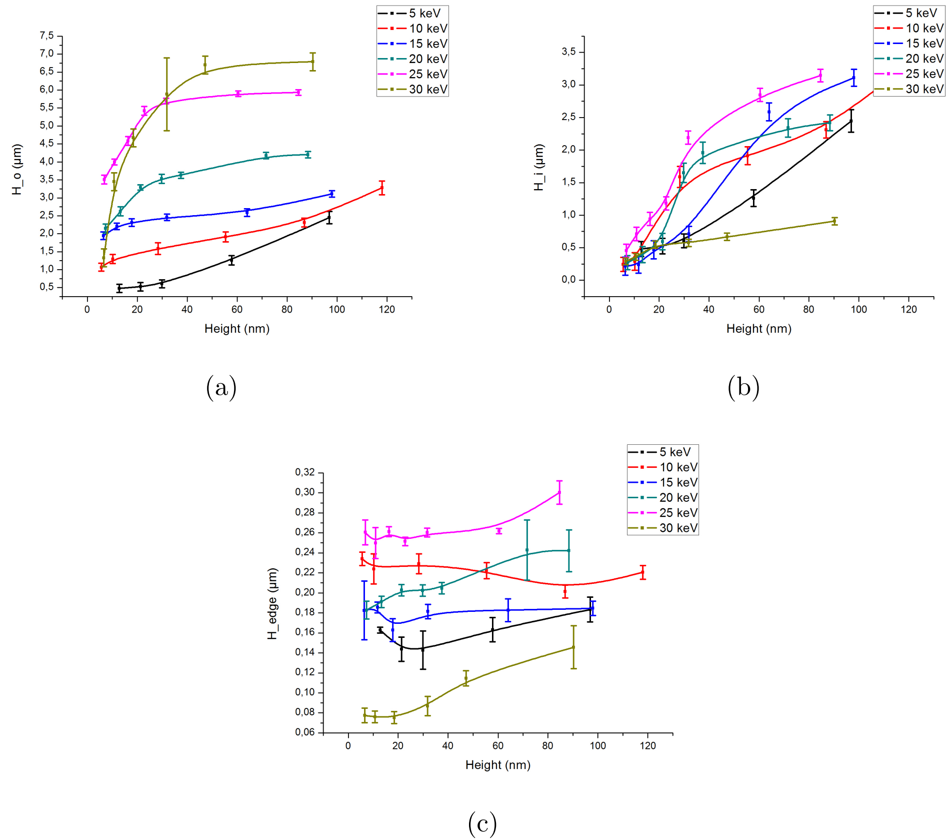

Figure 3.4: (a) Comparison of the outer halo H_o radius for the used acceleration voltages. (b) Comparison of the inner halo H_i radius for the used acceleration voltages. (c) Comparison of the edge halo H_{edge} radius for the used acceleration voltages.

can see the formation of an additional higher deposit with a defined edge. In the outer halo measurement, the blue plot in figure 3.4 (a), one can see an asymptotic behaviour for thin deposits up to approximately 30 nm height, which is dominated by BSE related deposition, whereas for higher deposits the outer halo is growing further, which indicates the change from BSE to FSE dominated deposition (see figure 3.4 (a)). The inner halo shows a steadily increasing radius, while the edge halo stays approximately the same for all deposit heights, as can be seen in figure 3.4 (c). So we come to the conlcusion, that the edge halo is an intrinsic process, which can't be optimized by parameter tuning, whereas the inner halo can be minimized by finding the optimal set of parameters.

At 5 keV only a broadening of the bottom of the structure has been observed, as shown in figure 2.11. This absence of an outer halo, as one can see at deposits with higher electron energies, and the small simulated radius of the BSE indicate, that for

these structures, the outer halo is dominated by the FSE and the inner halo radius is the same as the outer halo radius ranging from approximately 250 nm to 2.5 μm. As one can see, we have to deal with a different formation process of the outer halo for the sub-100 nm deposits at these electron energies: for high electron energies ($\geq$ 20 keV) and for thin deposits the outer halo is dominated by BSE, whereas for lower electron energies ($\leq$ 10 keV), the outer halo is formation is dominated by FSE. So one can see, that the halo formation is dependent on the electron energy as well as on the height of the deposit. Special attention, however, is needed for mid range energies ($\approx$ 15 keV) due to the strong height dependency, while high energy deposits are nearly independent on the height.

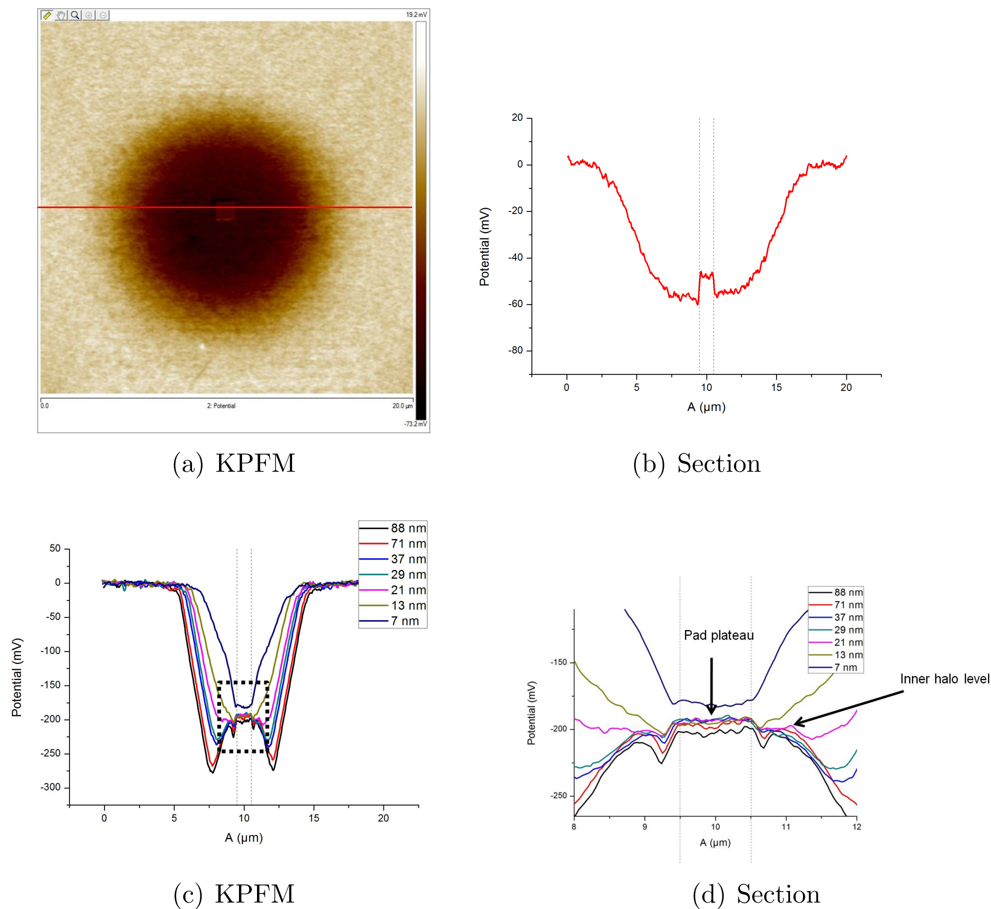

(a) KPFM (b) Section

(c) KPFM (d) Section

Figure 3.5: KPFM (a) and line section (b) image of investigated structure showing the forming of two plateaus, one at the pad itself and one at the halo. KPFM cross line section of 20 keV structures (c) and closer look to the center of the cross line section (d) for revealing the inner halo level.

Further investigations using Kelvin Probe Force Microscopy (**KPFM**) serve as tool

for distinguishing different chemical composition of deposited material. As one can see in figure 3.5, the pad and the outer halo form a different plateau suggesting strongly that the chemistry is different. Due to the lower plateau of the halo, substrate related effects can be excluded, as discussed in detail in section 2.1. These results allow for the conclusion, that the halo consists of incompletely dissociated intermediate products. For investigating the inner halo, one has to look at the 20 keV zoomed in cross line section, which can bee seen in figure 3.5. Out of this plot one can see that outside deposit edge, the level of the inner halo is similar to the deposit plateau, which leads to the conclusion, that the inner halo is formed of a similar chemical composition as the pad is. Considering the BSE/FSE change in dependency on the electron energy it is now obvious that the outer halo could show different properties for different dissociating electron species. Therefore, it is essential to focus on electrical measurements.

For revealing the conductivity of the different halos, a 5 keV deposit for investigating the FSE formed halo and a 30 keV deposit for investigating the BSE formed halo were observed. In figure 2.19 one can see the 30 keV structure, revealing that the outer halo formed by BSE is very little conductive, whereas in figure 2.20 one can see the 5 keV structure showing the inner halo formed by FSE to be conductive.

Hence, we conclude, that the limitation for lateral resolution is dominated by the inner halo H_i formed by FSE, which is conductive and has relative large dimensions for the sub-100 nm 5 keV deposits.

Out of these results, we can conclude a set of design rules for sub-100 nm deposits, at which the proximity effect are minimized. First of all it is important to state, that the different formation process of the inner and outer halo affects the conductivity: while the BSE formed halo is not conductive, the FSE formed halo is highly conductive and hence the most important one. The BSE formed halo is only relevant for high energies, due to the small surface radius of BSE for low energies, whereas the FSE formed halo has its minimum at high energies for these deposit heights. So we come to the conclusion, that deposits for the sub-100 nm height regime are suggestet to be fabricated with high primary electron energies. If this is impossible for some reasons, low energy deposits should be smaller than $\approx$ 20 nm.

This limitation in height makes it essential, that the thin deposits, which are less conductive, due to their small cross section, have to be postprocessed by e-beam curing to provide high conductivity, as recently demonstrated by Plank et. al. [30] .

4 Summary

The subject of this master thesis was the separation of design and process related influences from fundamental limitations and the subsequent formulation of design rules in the sub-100 nm height regime. For achieving these objectives, primary electron (PE) energies and deposit heights were systematically varied for revealing the evolution of the individual effects and finding optimal deposition parameters.

The unwanted effects could be subdivided into: 1) the edge halo H_{edge} as a result of secondary electron (SE) related broadening of the structure's side wall; 2) the outer halo H_o caused by substrate related backscattered electrons (BSE); and 3) the inner halo H_i which is formed by forward scattered electrons (FSE). Investigations via Kelvin probe force microscopy reveal that H_{edge} and H_i show very similar chemical composition compared to the actual deposit with a high fraction of fully dissociated precursor molecules. In contrast, the surface potential of H_o is found very different, which suggests strongly a high fraction of incompletely dissociated precursor molecules. This is further confirmed by C-AFM measurements, which reveal H_o as badly conductive, whereas H_{edge} and H_i show almost the same conductivity as the actual deposit.

By varying PE energies and deposit heights, it is found that the predominating electron species, responsible for halo formation, changes from BSE for high PE energies to FSE for low energies. Taking the conductivity measurements into account as well, which point out H_i as limiting proximity effect for conductive Pt deposits, we were able to define some fundamental design rules for enhancing the lateral resolution: first of all, it is suggested to deposit at high PE energies for sub-100 nm height regime, due to a weak dependency of H_i on deposit heights. Secondly, if low PE energies are required for some reasons, the deposit height should be as small as possible (ideally < 20 nm). This limitation, however, makes it essential that thin deposits have to be postprocessed by e-beam curring to provide highest conductivities.

References

[1] Utke, Ivo ; Hoffmann, Patrik ; Melngailis, John: Gas-assisted focused electron beam and ion beam processing and fabrication. In: *Journal of Vacuum Science & Technology B: Microelectronics and Nanometer Structures* 26 (2008), Nr. 4, 1197-1276. http://dx.doi.org/10.1116/1.2955728. – DOI 10.1116/1.2955728

[2] J. Goldstein, D. Newbury, D. Joy, C. Lyman, P. Echlin, E. Lifshin, L. Sawyer and J. Michael: *Scanning Electron Microscopy and X-ray Microanalysis*. Kluwer Academic, Plenum Publishers, New York, 2003

[3] Michelitsch, Stephan G.: *Electrical in situ measurements during electron beam induced platinum deposition*, Institute of Electron Microscopy, Graz University of Technology, Master Thesis, 2010

[4] *Specifications by FEI Company*. The Netherlands, www.feicompany.com

[5] Callegari, Victor ; Nellen, Philipp M.: Spontaneous growth of uniformly distributed In nanodots and InI3 nanowires on InP induced by a focused ion beam. In: *physica status solidi (a)* 204 (2007), Nr. 6, 1665–1671. http://dx.doi.org/10.1002/pssa.200675337. – DOI 10.1002/pssa.200675337. – ISSN 1862–6319

[6] Smith, D A. ; Fowlkes, J D. ; Rack, P D.: A nanoscale three-dimensional MonteCarlo simulation of electron-beam-induced deposition with gas dynamics. In: *Nanotechnology* 18 (2007), Nr. 26, 265308. http://stacks.iop.org/0957-4484/18/i=26/a=265308

[7] Fowlkes, Jason D. ; Rack, Philip D.: Fundamental Electron-Precursor-Solid Interactions Derived from Time-Dependent Electron-Beam-Induced Deposition Simulations and Experiments. In: *ACS Nano* 4 (2010), Nr. 3, 1619-1629. http://dx.doi.org/10.1021/nn901363a. – DOI 10.1021/nn901363a. – PMID: 20201541

[8] Smith, Daryl A. ; Fowlkes, Jason D. ; Rack, Philip D.: Understanding the Kinetics and Nanoscale Morphology of Electron-Beam-Induced Deposition via a

Three-Dimensional Monte Carlo Simulation: The Effects of the Precursor Molecule and the Deposited Material. In: *Small* 4 (2008), Nr. 9, 1382–1389. http://dx.doi.org/10.1002/smll.200701133. – DOI 10.1002/smll.200701133. – ISSN 1613–6829

[9] Plank, H ; Gspan, C ; Dienstleder, M ; Kothleitner, G ; Hofer, F: The influence of beam defocus on volume growth rates for electron beam induced platinum deposition. In: *Nanotechnology* 19 (2008), Nr. 48, 485302. http://stacks.iop.org/0957-4484/19/i=48/a=485302

[10] Smith, Daryl A. ; Fowlkes, Jason D. ; Rack, Philip D.: Simulating the effects of surface diffusion on electron beam induced deposition via a three-dimensional Monte Carlo simulation. In: *Nanotechnology* 19 (2008), Nr. 41, 415704. http://stacks.iop.org/0957-4484/19/i=41/a=415704

[11] Botman, A ; Mulders, J J L. ; Hagen, C W.: Creating pure nanostructures from electron-beam-induced deposition using purification techniques: a technology perspective. In: *Nanotechnology* 20 (2009), Nr. 37, 372001. http://stacks.iop.org/0957-4484/20/i=37/a=372001

[12] Utke, Ivo ; Friedli, Vinzenz ; Amorosi, Simone ; Michler, Johann ; Hoffmann, Patrik: Measurement and simulation of impinging precursor molecule distribution in focused particle beam deposition/etch systems. In: *Microelectronic Engineering* 83 (2006), Nr. 4-9, 1499 - 1502. http://dx.doi.org/DOI:10.1016/j.mee.2006.01.136. – DOI DOI: 10.1016/j.mee.2006.01.136. – ISSN 0167–9317. – Micro- and Nano-Engineering MNE 2005

[13] Matsui, Shinji ; Mori, Katsumi: New Selective Deposition Technology by Electron Beam Induced Surface Reaction. In: *Japanese Journal of Applied Physics* 23 (1984), Nr. Part 2, No. 9, L706-L708. http://dx.doi.org/10.1143/JJAP.23.L706. – DOI 10.1143/JJAP.23.L706

[14] Courtesy of Harald Plank, Steyrergasse 17, 8010 Graz, Austria: Institute for Electron Microscopy (FELMI-ZfE), Graz University of Technology,, www.felmi-zfe.at

[15] Allen, T. E. ; Kunz, R. R. ; Mayer, T. M.: Monte Carlo calculation of low-energy electron emission from surfaces. In: *Journal of Vacuum Science & Technology B: Microelectronics and Nanometer Structures* 6 (1988), Nr. 6, 2057-2060. http://dx.doi.org/10.1116/1.584111. – DOI 10.1116/1.584111

[16] Reimer, L.: *Scanning Electron Microscopy - Physics of Image Formation and*

Microanalysis. Bd. Volume 45. Berlin, Heidelberg : Springer Verlag, 1998

[17] DORP, Willem F. ; SOMEREN, Bob van ; HAGEN, Cornelis W. ; KRUIT, Pieter ; CROZIER, Peter A.: Approaching the Resolution Limit of Nanometer-Scale Electron Beam-Induced Deposition. In: *Nano Letters* 5 (2005), Nr. 7, 1303-1307. http://dx.doi.org/10.1021/nl050522i. – DOI 10.1021/nl050522i

[18] CHRISTOPHOROU, L.G. ; OLTHOFF, J.K.: Fundamental Electron Interactions with Plasma Processing Gases. In: *Kluwer Academic* 1st ed. (2004)

[19] FRIEDLI, V. et a.: In: *Abstracts of EIPBN '06, Baltimore* (2006)

[20] WEST, Dr. P.: *Introduction to Atomic Force Microscopy*. http://www.afmuniversity.org/download.html

[21] GARCIA, Ricardo: *Amplitude Modulation Atomic Force Microscopy*. Wiley-VCH, 2010

[22] BRUKER, AXS: *Application notes and manuals*, www.bruker-axs.com

[23] TEICHERT, Christian ; BEINIK, Igor ; BARAT, Bhushan (Hrsg.): *Scanning Probe Microscopy in Nanoscience and Nanotechnology*. Springer Verlag, 2010. – 691 – 721 S.

[24] JAHN, Birgit: *Morphological and electrostatic characterization of light emitting electrochemical cells by means of atomic force microscopy*, Institute of Solid State Physics, Graz University of Technology, Diploma Thesis, 2007

[25] PALERMO, V. ; PALMA, M. ; SAMOR, P.: Electronic Characterization of Organic Thin Films by Kelvin Probe Force Microscopy. In: *Advanced Materials* 18 (2006), Nr. 2, 145–164. http://dx.doi.org/10.1002/adma.200501394. – DOI 10.1002/adma.200501394. – ISSN 1521–4095

[26] LISCIO, Andrea ; PALERMO, Vincenzo ; MULLEN, Klaus ; SAMORI, Paolo: Tip-Sample Interactions in Kelvin Probe Force Microscopy: Quantitative Measurement of the Local Surface Potential. In: *The Journal of Physical Chemistry C* 112 (2008), Nr. 44, 17368-17377. http://dx.doi.org/10.1021/jp806657k. – DOI 10.1021/jp806657k

[27] MELITZ, Wilhelm ; SHEN, Jian ; KUMMEL, Andrew C. ; LEE, Sangyeob: Kelvin probe force microscopy and its application. In: *Surface Science Reports* 66 (2011), Nr. 1, 1 - 27. http://dx.doi.org/DOI:10.1016/j.surfrep.2010.10.001. – DOI

DOI: 10.1016/j.surfrep.2010.10.001. – ISSN 0167–5729

[28] Wnuk, Joshua D. ; Gorham, Justin M. ; Rosenberg, Samantha G. ; Dorp, Willem F. ; Madey, Theodore E. ; Hagen, Cornelis W. ; Fairbrother, D. H.: Electron Induced Surface Reactions of the Organometallic Precursor Trimethyl(methylcyclopentadienyl)platinum(IV). In: *The Journal of Physical Chemistry C* 113 (2009), Nr. 6, 2487-2496. http://dx.doi.org/10.1021/jp807824c. – DOI 10.1021/jp807824c

[29] Dorp, W. F. ; Wnuk, J. D. ; Gorham, J. M. ; Fairbrother, D. H. ; Madey, T. E. ; Hagen, C. W.: Electron induced dissociation of trimethyl, methylcyclopentadienyl. platinum, IV.: Total cross section as a function of incident electron energy. In: *JOURNAL OF APPLIED PHYSICS* 106 (2009), OCT 1, Nr. 7. http://dx.doi.org/{10.1063/1.3225091}. – DOI 10.1063/1.3225091. – ISSN 0021–8979

[30] H. Plank, C. Gspan A. Hohenau J. Krenn G. Kothleitner F. H. S.G.W. Michelitsch M. S.G.W. Michelitsch: *Optimization of postgrowth electron beam curing for focused electron beam induced Pt deposits.* – J. Vac. Scie. Techn. B, under second review, 2011

[31] Drouin, Dominique ; Couture, Alexandre R. ; Joly, Dany ; Tastet, Xavier ; Aimez, Vincent ; Gauvin, Raynald: CASINO V2.42 - A Fast and Easy-to-use Modeling Tool for Scanning Electron Microscopy and Microanalysis Users. In: *Scanning* 29 (2007), Nr. 3, 92–101. http://dx.doi.org/10.1002/sca.20000. – DOI 10.1002/sca.20000. – ISSN 1932–8745